



저작자표시-비영리-변경금지 2.0 대한민국

이용자는 아래의 조건을 따르는 경우에 한하여 자유롭게

- 이 저작물을 복제, 배포, 전송, 전시, 공연 및 방송할 수 있습니다.

다음과 같은 조건을 따라야 합니다:



저작자표시. 귀하는 원저작자를 표시하여야 합니다.



비영리. 귀하는 이 저작물을 영리 목적으로 이용할 수 없습니다.



변경금지. 귀하는 이 저작물을 개작, 변형 또는 가공할 수 없습니다.

- 귀하는, 이 저작물의 재이용이나 배포의 경우, 이 저작물에 적용된 이용허락조건을 명확하게 나타내어야 합니다.
- 저작권자로부터 별도의 허가를 받으면 이러한 조건들은 적용되지 않습니다.

저작권법에 따른 이용자의 권리는 위의 내용에 의하여 영향을 받지 않습니다.

이것은 [이용허락규약\(Legal Code\)](#)을 이해하기 쉽게 요약한 것입니다.

[Disclaimer](#)

공학석사 학위논문

Tailoring the Porosity of Metal-Organic
Framework-Derived N-doped Carbon
Electrocatalysts for High-Performance
Dye-Sensitized Solar Cells

고성능 염료감응태양전지를 위한
금속유기구조체 유래의 질소가 도핑된
탄소 전기촉매의 기공성 조절

2019년 2월

서울대학교 대학원

화학생물공학부 에너지환경화학융합기술전공

강 지 호

Abstract

Tailoring the Porosity of Metal-Organic Framework-Derived N-doped Carbon Electrocatalysts for High-Performance Dye-Sensitized Solar Cells

Jiho Kang

Chemical Convergence for Energy & Environment

School of Chemical and Biological Engineering

The Graduate School

Seoul National University

Metal-organic framework (MOF)-derived carbon materials have been widely used as catalysts for a variety of electrochemical energy applications, and thermally carbonized zinc-2-methylimidazole (ZIF-8) has shown particularly high performance owing to its microporous structure with a large surface area. However, in the presence of bulky chemical species, such as triiodide in

mesoscopic dye-sensitized solar cells (DSCs), the small pore size of carbonized ZIF-8 causes a significant limitation in mass transfer and consequentially results in a poor performance. In this research, a simple strategy to resolve the issue is introduced, in which the pore sizes of ZIF-8-derived carbon are enlarged by increasing the dwelling time of Zn in ZIF-8 during the thermal carbonization process. A thin and uniform polydopamine shell introduced on the surface of ZIF-8, with the aim of retarding the escape of vaporized Zn species, leads to a dramatic increase in pore sizes, from the micropore to mesopore range. The porosity-tailored carbonized ZIF-8 manifests an excellent electrocatalytic performance in triiodide reduction, and when it is applied as the counter electrode of DSCs, an energy conversion efficiency of up to 9.03% is achievable, which is not only superior to that of the Pt-based counterpart but also among the highest performances of DSCs employing carbonaceous electrocatalysts.

Keywords: dye-sensitized solar cells, counter electrodes, triiodide reduction reaction, mass transfer resistance, metal-organic frameworks, pore size-tuning, polydopamine

Student Number: 2017-28143

Contents

Abstract	1
Contents	3
List of Tables	4
List of Figures	5
1. Introduction	9
2. Experimental	
2.1. Preparation of CEs employing ZIF-8-C or ZIF-8-dopa-C	13
2.2. Assemblies of symmetric cells and mesoscopic solar cells	14
2.3. Materials characterizations and (Photo)electrochemical measurements	15
3. Results and Discussion	
3.1. Synthesis and physical characterization	17
3.2. Electrochemical performance for triiodide reduction	34
3.3. Analyses on kinetics by factors	41
3.4. Comparisons of intrinsic activities	54
3.5. Applications in mesoscopic solar cells	61
4. Conclusions	69
References	70
국문초록 (Korean Abstract)	77

List of Tables

Table 3.1.1. Summary of fitting results for XPS (a) carbon 1s and (b) nitrogen 1s spectra of ZIF-8-C and ZIF-8-dopa-C.	33
Table 3.3.1. Summary of fitting results for EIS spectra of the symmetric cells employing (a) platinum, (b) ZIF-8-C, and (c) ZIF-8-dopa-C electrodes.	45
Table 3.4.1. Exchange current densities in the symmetric cells employing platinum, ZIF-8-C, or ZIF-8-dopa-C at diverse temperatures and the corresponding activation energies calculated using Arrhenius equation.	57
Table 3.5.1. Fill factors and power conversion efficiencies of DSCs employing carbon-based CEs reported in previous publications and from our experiment. The comparison on the performances is limited to the N719 dye- and I_3^-/I^- redox electrolyte-based cells for proper evaluations.	64
Table 3.5.2. Summary of $J-V$ characteristics for DSCs employing $[\text{Co}(\text{bpy})_3]^{3+/2+}$ redox electrolyte and platinum, ZIF-8-C, and ZIF-8-dopa-C CEs.	67

List of Figures

Figure 3.1.1. Schematic illustration for the preparation steps of ZIF-8-derived N-doped carbons.	18
Figure 3.1.2. SEM images of (a-d) ZIF-8-C and (e-h) ZIF-8-dopa-C.	19
Figure 3.1.3. TEM images of (a) ZIF-8-C and (b) ZIF-8-dopa-C. The insets show elemental mapping results for carbon and nitrogen.	20
Figure 3.1.4. (a-d) TEM images of ZIF-8-C obtained at diverse magnifications.	22
Figure 3.1.5. (a-d) TEM images of ZIF-8-dopa-C obtained at diverse magnifications.	23
Figure 3.1.6. (a) XRD patterns of the ZIF-8-derived N-doped carbons with that of pristine ZIF-8 displayed in the inset. (b) N ₂ -sorption isotherms of ZIF-8-C and ZIF-8-dopa-C, and the BJH pore distributions (inset).	24
Figure 3.1.7. (a,b) TGA curves of ZIF-8 and ZIF-8-dopa measured (a) from room temperature to 800 °C at the rate of 5 °C/min followed by (b) temperature maintenance at 800 °C for 2 h.	27
Figure 3.1.8. Schematic illustration showing the impeded escape of Zn vapors from ZIF-8-dopa compared to ZIF-8 during the thermal carbonization.	28

Figure 3.1.9. (a) Carbon K-edge XAS data and (b) XPS N 1s spectra of the ZIF-8-derived N-doped carbons.	30
Figure 3.1.10. (a) XPS C 1s spectra of ZIF-8-C and ZIF-8-dopa-C and (b,c) their fitted results; (b) ZIF-8-C and (c) ZIF-8-dopa-C.	31
Figure 3.1.11. XPS N 1s spectra of (a) ZIF-8-C and (b) ZIF-8-dopa-C and their fitted results.	32
Figure 3.2.1. (a) CV diagrams of platinum, ZIF-8-C, and ZIF-8-dopa-C CEs. Data from 10th cycle were depicted for comparisons. (b-d) 100 cycles of CV for (b) platinum, (c) ZIF-8-C, and (d) ZIF-8-dopa-C CEs.	37
Figure 3.2.2. Peak current densities vs. (scan rate) ^{1/2} plots of Pt, ZIF-8-C, and ZIF-8-dopa-C obtained from the I ₃ ⁻ /I ⁻ peak of the CV data measured at various scan rates (30, 60, 90, 120, 150 mV/s).	38
Figure 3.2.3. (a) Tafel polarization curves of symmetric cells employing platinum, ZIF-8-C, or ZIF-8-dopa-C, and (b) polarization curves of the same symmetric cells near zero-voltage region.	40
Figure 3.3.1. (a-c) Nyquist plots of the symmetric cells employing (a) platinum, (b) ZIF-8-C, and (c) ZIF-8-dopa-C measured at diverse temperatures. (d,e) Parameters obtained by fitting the EIS data; (d) charge transfer resistance and (e) diffusion resistance.	42
Figure 3.3.2. Equivalent circuit for EIS analyses of symmetric cells.	43

Figure 3.3.3. Enlarged Nyquist plots of the symmetric cells employing (a) Pt, (b) ZIF-8-C, and (c) ZIF-8-dopa-C CEs near the high-frequency region.	44
Figure 3.3.4. CV diagrams showing the specific capacitance vs. potential plots for (a) ZIF-8-C and (b) ZIF-8-dopa-C measured at diverse scan rates using 1.0 M NaCl electrolyte.	49
Figure 3.3.5. CV diagrams showing the specific capacitance vs. potential plots for (a) ZIF-8-C and (b) ZIF-8-dopa-C measured at diverse scan rates using 1.0 M NaClO ₄ electrolyte.	50
Figure 3.3.6. Capacity retentions of ZIF-8-C and ZIF-8-dopa-C for the cases of (a) 1.0 M NaCl and (b) 1.0 M NaClO ₄ electrolytes.	51
Figure 3.3.7. Schematic illustration of electrocatalytic reduction of triiodide at the surface of (a) microporous ZIF-8-C and (b) mesoporous ZIF-8-dopa-C.	52
Figure 3.4.1. Arrhenius plot of the symmetric cells constructed by calculation of exchange current densities using the geometric area-normalized charge transfer resistance values.	56
Figure 3.4.2. Raman spectra of (a) ZIF-8-C and (b) ZIF-8-dopa-C.	60

Figure 3.5.1. (a) $J-V$ curves of DSCs employing platinum, ZIF-8-C, or ZIF-8-dopa-C CEs measured under standard 1 sun illumination (AM 1.5G condition). (b) IPCE spectra of the same DSCs. 63

Figure 3.5.2. $J-V$ curves of DSCs employing $[\text{Co}(\text{bpy})_3]^{3+/2+}$ redox electrolyte and platinum, ZIF-8-C, and ZIF-8-dopa-C CEs measured under standard 1 sun illumination (AM 1.5G condition). 66

Chapter 1. Introduction

On account of rapidly growing demands on renewable and sustainable energy sources, great efforts have been put to the development of highly efficient solar cells. Among various types of photovoltaics, dye-sensitized solar cells (DSCs) have gained attention owing to their reliable performance, economic feasibility, and wide range of possible applications.¹⁻⁶ DSCs are generally driven by a mesoscopic TiO₂ photoelectrode with visible light-absorbing dyes on the surface, and a counter electrode (CE) is used for electrocatalytic regeneration of redox species (typically triiodide/iodide, I₃⁻/I⁻) in the electrolyte.⁷⁻⁹ These redox couples subsequently restore charges to the photoelectrodes, constituting the complete electrical circuit for solar-to-electrical energy conversion. Though overall performance of DSCs is dominated by light harvesting and charge collection efficiency of the photoelectrodes, CEs are responsible for a significant portion of manufacturing cost due to the usage of noble metal catalysts such as platinum.⁹⁻¹³ Various low-cost materials have been suggested as candidates to replace Pt, and meaningful progresses were made by using carbonaceous materials,¹⁴⁻¹⁸ conductive polymers,¹⁹⁻²² and inorganic compounds with diverse compositions and architectures.²³⁻³⁰

Recently, among various nanostructured composites,³¹⁻³⁶ metal-organic framework (MOF)-derived materials have been intensively studied in electrochemical energy conversion and storage, for MOFs have a number of favorable characteristics such as porous structure with high uniformity and large variety of possible compositions.^{37,38} In DSCs, nanostructured sulfides synthesized using MOFs were first applied as electrocatalysts in CEs,³⁹ followed by the reports on numerous MOF-based composites with decent performances.⁴⁰⁻⁴⁵ Meanwhile, in other fields of electrochemical applications, nitrogen-doped microporous carbons prepared by thermal carbonization of Zn-containing zeolitic imidazolate framework (ZIF), typically zinc-2-methylimidazole (ZIF-8), have been widely used.⁴⁶⁻⁴⁸ Unlike other metals in MOFs, Zn vaporizes during the thermal carbonization and forms microporous carbon with a large available surface area.^{49,50} In addition, it has high N-content due to the presence of imidazole in the framework that serves as a rich N source. As a result, ZIF-8-derived carbons provide large number of active catalytic sites for various electrochemical reactions, and oxygen reduction reaction for fuel cells is a typical example.⁵¹⁻⁵⁴ Carbonized ZIF-8 was also applied as CE materials for DSCs, and energy conversion efficiency slightly lower than Pt counterpart was obtained.⁵⁵ Given that numerous types of carbonaceous materials manifested superior performances compared to

that of Pt, it could be presumed that carbonized ZIF-8 has some limitation in electrocatalytic reduction of triiodides.^{13,18} Large surface area of carbon-based electrocatalysts and the presence of N-dopants are known to increase the number of active sites and their activities, and thus the shortcoming of carbonized ZIF-8 was more likely to result from its structural property, which has significant influence on the mass transfer of redox species. The length of I_3^- is known to be approximately 1 nm,⁵⁶ which is a significantly larger size than those of chemical species for which carbonized MOF exhibit excellent performances. Therefore, insufficient pore size for facile movements of I_3^-/I^- redox couples was suspected as one of the most probable reasons.

As stated above, vaporization of Zn during the thermal carbonization of ZIF-8 leads to the formation of micropores. It is also widely known that Zn species serve as porogens in thermal carbonization of various organic and polymeric materials,⁵⁷⁻⁶⁰ and increased amount of Zn present in the carbon precursors augments the size of pores even up to mesoscale.^{57,58} Yu et al. recently verified that enlargement of pore size occurs as a result of ZnO formation prior to vaporization, which accompanies deoxygenation of carbon precursors and promotes graphitization of resulting carbon materials.⁶¹ However, since Zn constitutes the periodic framework of ZIF-8, its content cannot be increased further. Therefore, pore sizes of the resulting carbon are

restricted to micropore range, which is unfavorable for the mass transfer of the redox species. In this study, a simple strategy to enlarge the pore sizes of ZIF-8-derived carbons is suggested, which maximizes the influence of Zn within ZIF-8 during the carbonization process. A thin and uniform polydopamine shell is introduced on the surface of ZIF-8 in order to elongate the dwelling time of Zn within ZIF-8 before the escaping of vaporized Zn, which engenders the formation of open-pore structures. As a result, the pore size of the resulting N-doped carbon was increased to the mesopore range, and these porosity-tailored ZIF-8-derived carbon led to a significantly enhanced electrocatalytic performance in triiodide reduction. When the synthesized N-doped carbon with enlarged pores was applied as a CE material in DSCs, energy conversion efficiency up to 9.03% was achieved, which was a superior value compared to those obtained by using carbonized ZIF-8 (8.34%) and state-of-the-art Pt (8.85%).

Chapter 2. Experimental

2.1. Preparation of CEs employing ZIF-8-C or ZIF-8-dopa-C

ZIF-8 used in this study was purchased from Sigma-Aldrich (Basolite® Z1200). Polydopamine coating was carried out in a buffer solution (pH 8.5) containing 10 mM of dopamine hydrochloride (Sigma-Aldrich) for 2 h with a mild stirring. ZIF-8 and ZIF-8-dopa were thermally carbonized in an Ar-filled tube at 800 °C for 2 h followed by acid treatment to remove the remaining Zn within the prepared ZIF-8-C and ZIF-8-dopa-C. These carbons were deposited on FTO glasses (TEC-8, Pilkington) by spraying them in the form of ink, wherein isopropanol and Nafion were used as solvent and binders, respectively, followed by heat treatment at 500 °C in Ar for 4 h to improve the connectivity between the carbon particles. The amount of Nafion binder in the catalyst ink was 1/10 of the ZIF-derived N-doped carbon by weight. Electrodes for capacitance retention measurements were fabricated by blending ZIF-derived N-doped carbons, carbon black conducting agent (Timcal), and polytetrafluoroethylene binder (Sigma-Aldrich) in mass ratio of 8:1:1, respectively. Then, the mixture was kneaded in a pestle, pressed in a roll press machine, and dried in vacuum oven. Platinum CEs were prepared by spin-casting of isopropanol containing 50 mM of H_2PtCl_6 on FTO glasses

followed by heat treatment at 400 °C for 20 min in air.

2.2 Assemblies of symmetric cells and mesoscopic solar cells

Symmetric cells were assembled using identical CEs with the assistance of 50 µm-thick thermoplastic sealants (Surlyn, Dupont), and the I_3^-/I^- redox electrolyte prepared by mixing 0.6 M 1-butyl-3-methylimidazolium iodide, 30 mM I_2 , 0.1 M guanidinium thiocyanate, and 0.5 M 4-*tert*-butylpyridine in a mixed solution of acetonitrile and valeronitrile ($v/v = 85:15$) was injected into the cells through pre-drilled holes. Mesoscopic TiO_2 photoelectrodes for DSCs were prepared by sequentially doctor blading commercial pastes containing colloidal TiO_2 nanoparticles (DSL 18NR-T, Dyesol) and scattering particles (WER2-O, Dyesol) onto FTO glass substrates coated with TiO_2 blocking layer. The photoelectrodes underwent thermal sintering at 500 °C in air for 30 min and $TiCl_4$ post-treatment to increase the surface area and enhance the electron injection into TiO_2 conduction band.⁹⁰ Dye-sensitization was carried out by immersing the TiO_2 electrodes in ethanolic solution of 0.5 mM N719 sensitizer (D719, Everlight Chemicals) at 30 °C for 48 h. DSCs were prepared by assembling a photoelectrode and a counter electrode followed by injection of electrolyte using the identical method as for the case of symmetric cells. For the preparation of DSCs employing $[Co(bpy)_3]^{3+/2+}$

redox electrolyte, Y123 dye (DN-F05Y, Dyenamo) was used as the sensitizer, and an acetonitrile solution containing 0.22 M $\text{Co}(\text{bpy})_3(\text{PF}_6)_2$ (DN-C01, Dyenamo), 0.033 M $\text{Co}(\text{bpy})_3(\text{PF}_6)_3$ (DN-C02, Dyenamo), 0.1 M LiClO_4 , and 0.2 M 4-tert-butylpyridine was used as the electrolyte.

2.3. Materials characterizations and (photo)electrochemical measurements

SEM and TEM analyses were carried out using a Carl Zeiss AURIGA and a FEI Tecnai F20, respectively. N_2 sorption experiments were performed using a Micromeritics ASAP 2020. XRD patterns were obtained using a Rigaku D-MAX2500-PC equipped with a $\text{Cu-K}\alpha$ radiation source, and XPS spectra were measured using a Thermo SIGMA PROBE with an $\text{Al-K}\alpha$ source. XAS analysis was carried out at 4D Beamline of Pohang Accelerator Laboratory (PAL) in Republic of Korea. TGA measurements were carried out using a SDT-Q600 (TA Instruments). Raman spectra were collected using a Horiba Jobin-Yvon LabRam Aramis spectrometer, where 514 nm line of an Ar-ion laser was used as the excitation source. CV analyses were carried out by using a potentiostat (Autolab PGSTAT, Metrohm). A graphite rod CE, an Ag/AgNO_3 reference electrolyte counter electrode, and an acetonitrile electrolyte containing 10 mM LiI , 1 mM I_2 , and 0.1 M LiClO_4 were used for

the CV measurements. EIS measurements were carried out by using a ZIVE MP1 with sinusoidal perturbations of 10 mV. The capacitance retention measurements were conducted by using a potentiostat (VersaSTAT3, Princeton Applied Research) in a three electrode configuration based on an activated carbon-based CE, an Ag/AgCl (sat. KCl) reference electrode, and a cellulose nitrate membrane separator. Photovoltaic performances of the prepared DSCs were evaluated under simulated AM 1.5G illumination (light intensity: 100 mW/cm²) by using a solar simulator (XIL model 05A50KS source measure units), and the J – V data were collected by a potentiostat (1480 Multistat, Solartron). IPCEs measurements were carried out using a QEX7 device (PV Measurements).

Chapter 3. Results and Discussion

3.1. Synthesis and physical characterization

As depicted in Figure 3.1.1, ZIF-derived N-doped carbons were prepared by thermal carbonization of pristine ZIF-8 particles with or without polydopamine shells. Polydopamine coating on ZIF-8 was carried out by immersing the ZIF-8 particles in a buffer solution (pH 8.5) containing 10 mM of dopamine hydrochloride, followed by a mild stirring for 2 h. Pristine ZIF-8 and polydopamine-coated ZIF-8 (ZIF-8-dopa) were then thermally carbonized in Ar atmosphere at 800 °C for 2 h. The carbonized ZIF-8 (ZIF-8-C) and ZIF-8-dopa (ZIF-8-dopa-C) were first characterized by electron microscopy. Figures 3.1.2a-d display the scanning electron microscopy (SEM) images of ZIF-8-C, where the carbonized particles with a slightly shrunk structure from the polyhedral morphologies of ZIF-8 are observable. Meanwhile, the SEM images in Figures 3.1.2e-h show that ZIF-8-dopa-C particles have a similar structure but with more rounded edges attributable to the polydopamine shells. Figure 3.1.3 shows the transmission electron microscopy (TEM) images of the ZIF-8-C (Figure 3.1.3a) and ZIF-8-dopa-C (Figure 3.1.3b). The morphologies of the ZIF-derived carbons in TEM images

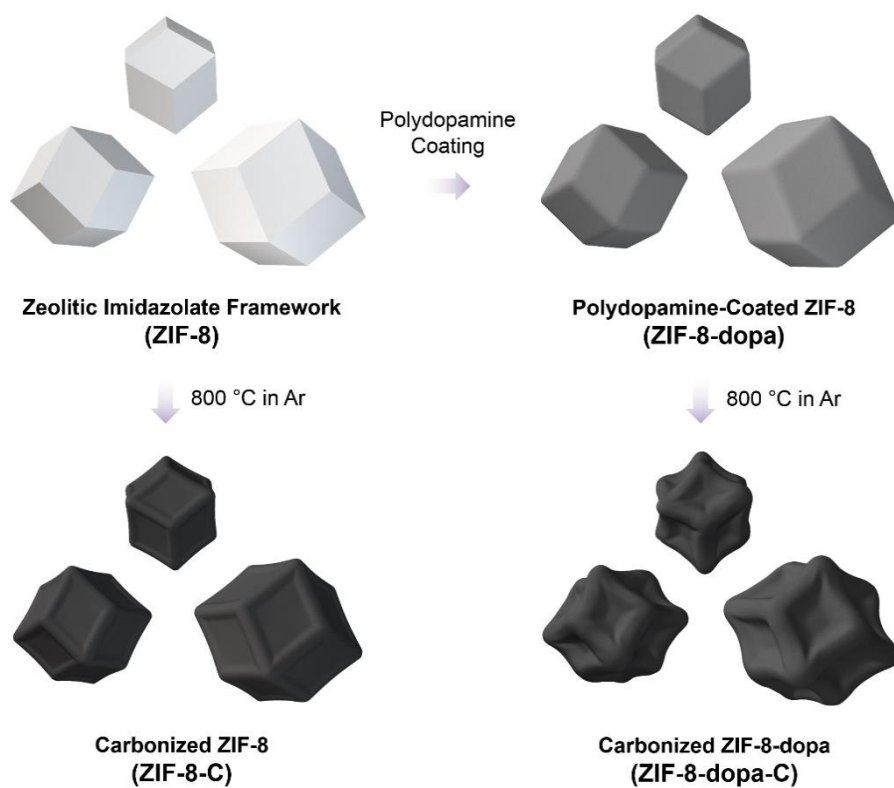


Figure 3.1.1. Schematic illustration for the preparation steps of ZIF-8-derived N-doped carbons.

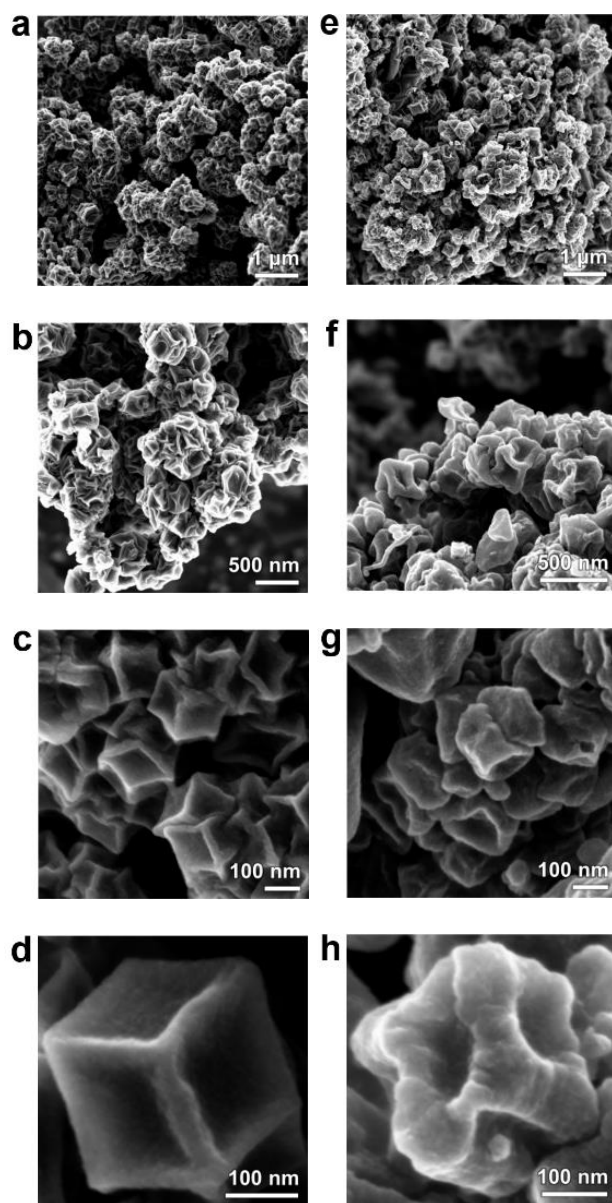


Figure 3.1.2. SEM images of (a-d) ZIF-8-C and (e-h) ZIF-8-dopa-C.

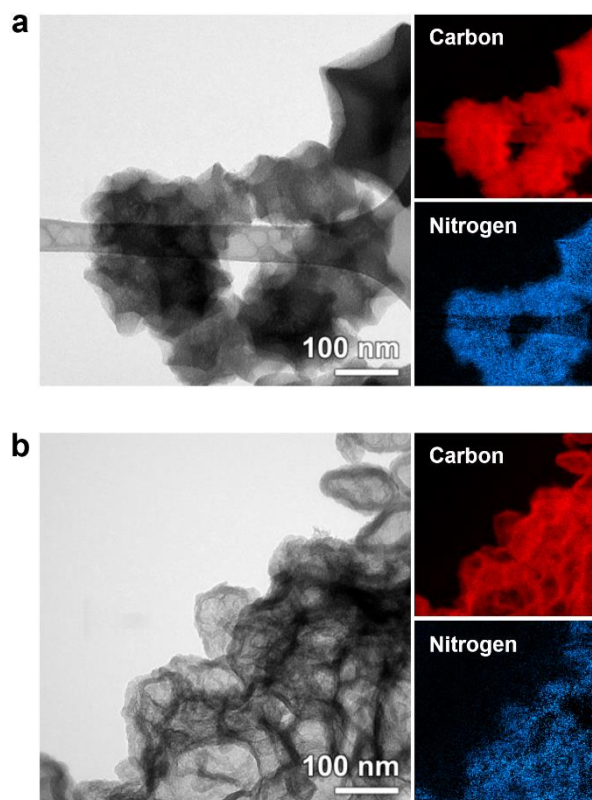


Figure 3.1.3. TEM images of (a) ZIF-8-C and (b) ZIF-8-dopa-C. The insets show elemental mapping results for carbon and nitrogen.

matched well with those from the SEM analyses, and approximately 20 nm-thick shells were clearly observable in the outer parts of ZIF-8-dopa-C. Elemental maps of carbon and nitrogen were additionally obtained based on electron energy loss spectroscopy (EELS) technique, and the images are displayed as the insets of Figure 3.1.3. Both C and N were uniformly distributed in ZIF-8-C, but for ZIF-8-dopa-C, signals from carbon were relatively stronger at the shell and larger amount of nitrogen at the core was noted. This difference is attributable to the dissimilar C and N compositions in the precursors; N content of imidazolate in ZIF-8 is higher than that of polydopamine. Moreover, amorphous characteristics of the ZIF-derived carbons were recognizable from the TEM images of diverse magnifications (see Figures 3.1.4 and 3.1.5 for ZIF-8-C and ZIF-8-dopa-C, respectively).

ZIF-derived N-doped carbons were then analyzed by X-ray diffraction (XRD), of which results are depicted in Figure 3.1.6a. Given that pristine ZIF-8 particles have numerous diffraction peaks originated from their highly periodic structure (see the inset of Figure 3.1.6a), which also matched well with the simulated XRD patterns,^{62,63} it could be verified from the XRD results that ZIF-8 and ZIF-8-dopa were completely transformed into amorphous carbons during the heat treatment. Figure 3.1.6b displays the N₂ sorption analysis results of the ZIF-derived N-doped carbons, from which

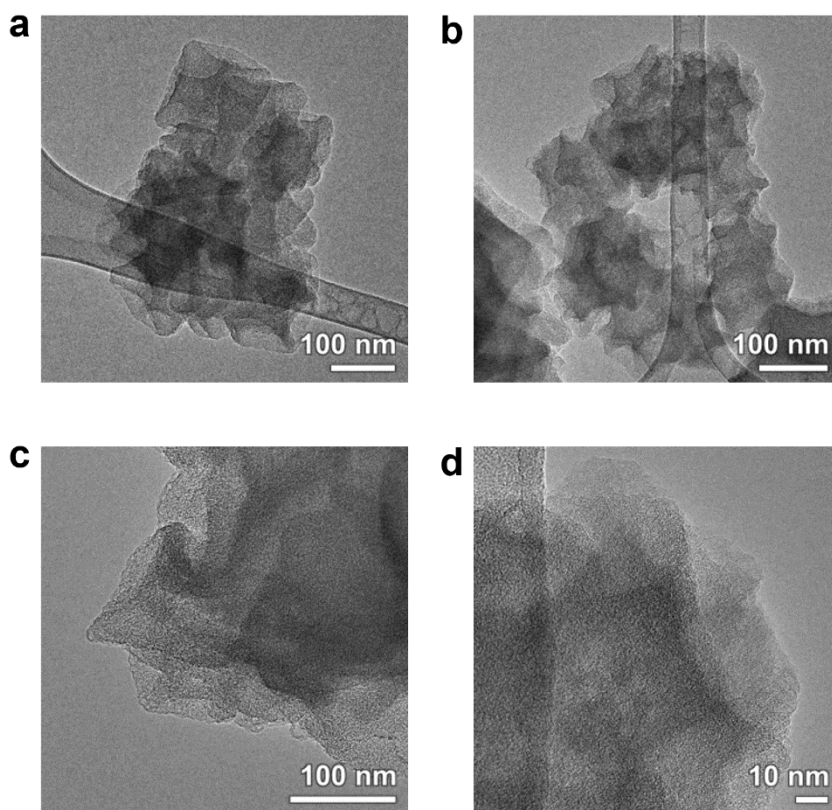


Figure 3.1.4. (a-d) TEM images of ZIF-8-C obtained at diverse magnifications.

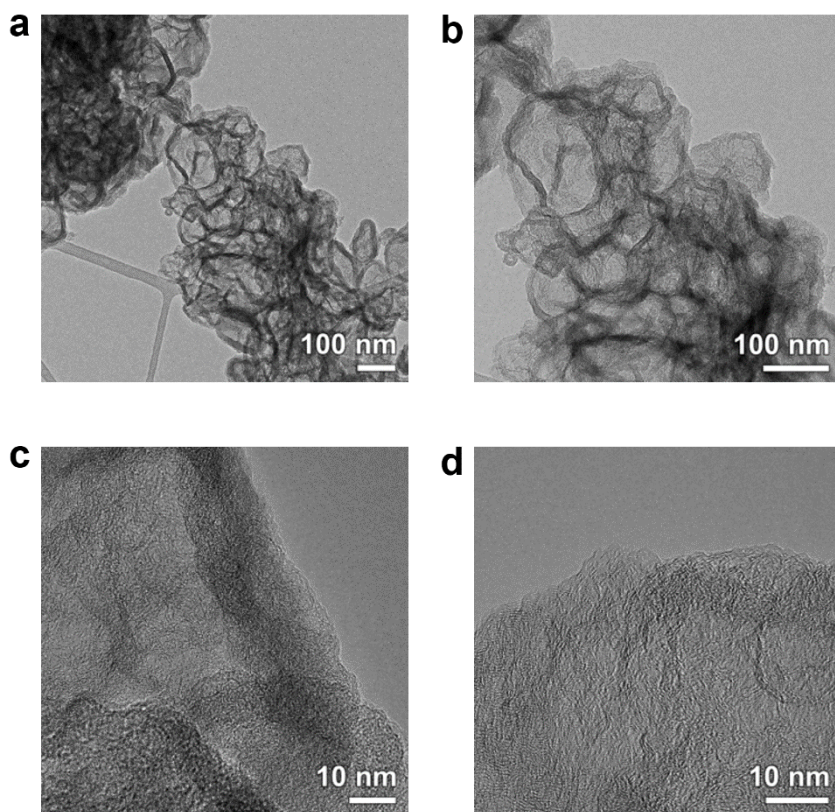


Figure 3.1.5. (a-d) TEM images of ZIF-8-dopa-C obtained at diverse magnifications.

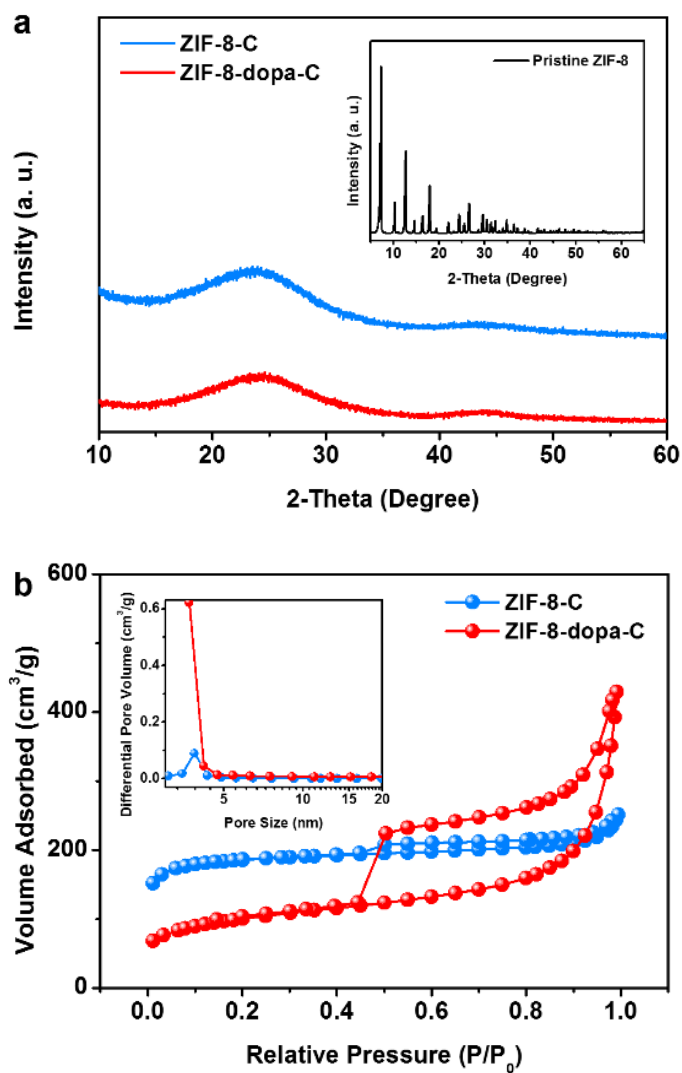


Figure 3.1.6. (a) XRD patterns of the ZIF-8-derived N-doped carbons with that of pristine ZIF-8 displayed in the inset. (b) N₂-sorption isotherms of ZIF-8-C and ZIF-8-dopa-C, and the BJH pore distributions are depicted in the inset.

Brunauer-Emmett-Teller (BET) surface areas of ZIF-8-C and ZIF-8-dopa-C were obtained as 629.22 m²/g and 353.69 m²/g, respectively. ZIF-8-C showed a typical Type I isotherm, indicating that majority of its pores are micropores. Meanwhile, I,IV-hybrid type isotherm was observed in the case of ZIF-8-dopa-C, verifying the presence of mesopores in ZIF-8-dopa-C, which seems to be the main reason for the smaller BET surface area. From the pore distributions of the ZIF-derived N-doped carbons calculated by Barret-Joyner-Halenda (BJH) method (see the inset of Figure 3.1.5b), it was notable to observe that mesopores were well-developed in ZIF-8-dopa-C, while ZIF-8-C had negligible pore volumes in that region.

As mentioned in the introduction, influence of Zn in thermal carbonization procedures was reported as facilitation of carbon graphitization and deoxygenation (ZnO formation), which consequentially lead to an increased pore size after removal of Zn species.⁶¹ It is also widely known that the pore size can be increased by adding larger amount of Zn salts to the precursors for carbon synthesis.^{57,58} Considering that there are no pore-forming agents in ZIF-8 and ZIF-8-dopa other than Zn in the frameworks and that the only difference between them is the presence of the polydopamine layer, promoted formation of mesopores in ZIF-8-dopa-C is ascribable to the increased influence of Zn on the resulting carbon owing to the shell on the

surface. Since polydopamine coating process first generates a dense layer on the surface,^{64,65} vaporized Zn seems to escape from ZIF-8-dopa at a slower rate during the thermal carbonization when compared with the case of ZIF-8. In order to verify this, thermogravimetric analysis (TGA) was carried out in Ar atmosphere. Figures 3.1.7a and b shows the TGA curves of ZIF-8 and ZIF-8-dopa measured in an identical condition to the thermal carbonization process; elevation of temperature at the rate of 5 °C/min up to 800 °C followed by the temperature maintenance at 800 °C for 2 h. As depicted in Figure 3.1.7a, the weight of ZIF-8-dopa gradually decreased as soon as the temperature exceeded the room temperature) while ZIF-8 did not manifest a significant weight loss until ~600 °C. The different behaviors between ZIF-8 and ZIF-8-dopa seem to be caused by the properties of polydopamine shells, as the polydopamine shells without ZIF-8 (removed by an acid treatment) manifested substantial drop in weight as the temperature was increased from 25 to 600 °C (Figure 3.1.7c). On the other hand, in the temperature above 600 °C, the weight of ZIF-8 showed a steeper decrease, and the relative weight changes of ZIF-8 and ZIF-8-C crossed their values soon after reaching at the temperature of 800 °C (Figure 3.1.7b). This observation clearly shows that the dwelling time of Zn was elongated by the presence of polydopamine shells, increasing the (pore-enlarging) influence of Zn and giving rise to the

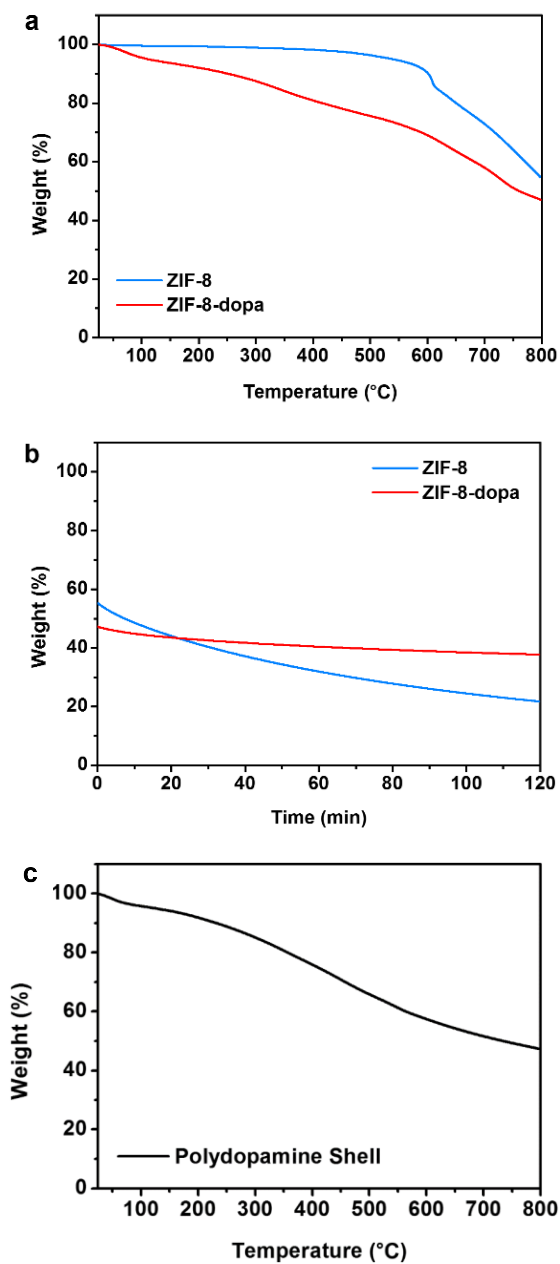


Figure 3.1.7. (a,b) TGA curves of ZIF-8 and ZIF-8-dopa measured (a) from room temperature to 800 °C at the rate of 5 °C/min followed by (b) temperature maintenance at 800 °C for 2 h. (c) TGA curve of polydopamine shell prepared by removal of ZIF-8 from ZIF-8-dopa.

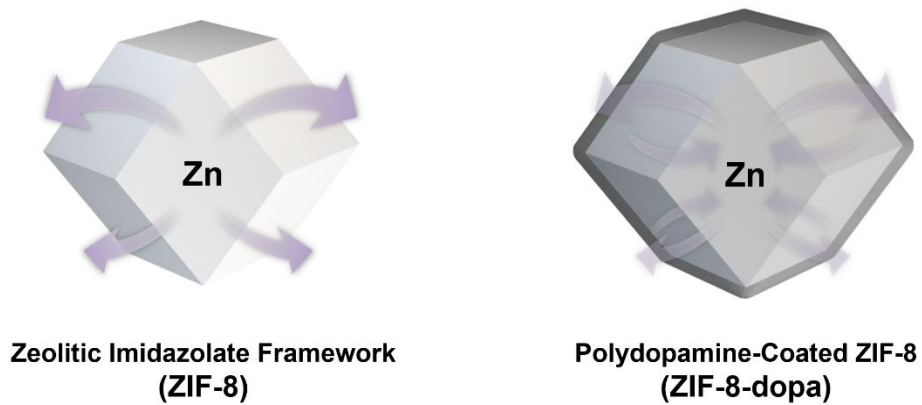


Figure 3.1.8. Schematic illustration showing the impeded escape of Zn vapors from ZIF-8-dopa compared to ZIF-8 during the thermal carbonization.

formation of mesopores, as schematically illustrated in Figure 3.1.8.

Figure 3.1.9a shows the X-ray absorption spectroscopy (XAS) data of ZIF-8-C and ZIF-8-dopa-C at carbon *K*-edge. In general, signals from around 285.3 and 293.0 eV are known to originate from sp^2 - and sp^3 -carbons, respectively, and the peak located at 288.5 eV is related to carbons bonded to oxygen or nitrogen.^{66,67} From the X-ray photoelectron spectroscopy (XPS) C 1s spectra (Figure 3.1.10), it could be verified that the degree of carbon oxidation is similar in ZIF-8-C and ZIF-8-dopa-C, though ZIF-8-dopa-C showed a slightly larger amount of oxygen near the surface (see Table 1a and Figure 3.1.10).^{68,69} Therefore, a smaller XAS peak from ZIF-8-dopa-C at 288.5 eV could be attributed to a lower N content of ZIF-8-dopa-C when compared with ZIF-8-C. This was additionally confirmed by XPS N 1s spectra (Figure 3.1.9b), which showed that significantly larger amount of nitrogen is present in the surface of ZIF-8-C than for the case of ZIF-8-dopa-C. As previously observed from the elemental maps of ZIF-8-dopa-C (in Fig. 3.1.3b), the N content in the ZIF-8-derived internal part is higher than that in the polydopamine-based shell, and this is in line with the XPS data which dominantly shows the signals from the surface. The XPS N 1s spectra were fitted according to three types of nitrogen (pyridinic, pyrrolic, and graphitic),^{70,71} and the detailed results are displayed in Table 3.1.1b and

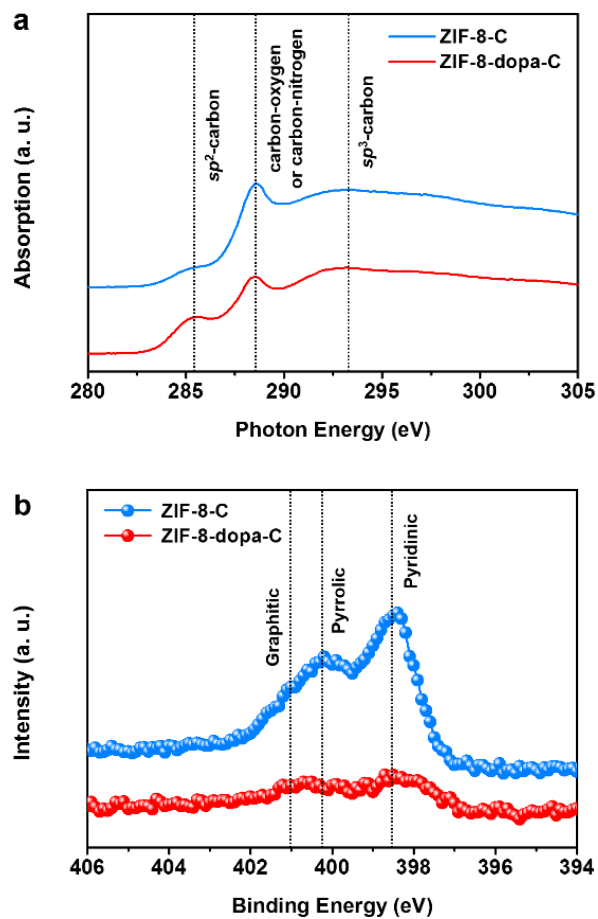


Figure 3.1.9. (a) Carbon K-edge XAS data and (b) XPS N 1s spectra of the ZIF-8-derived N-doped carbons.

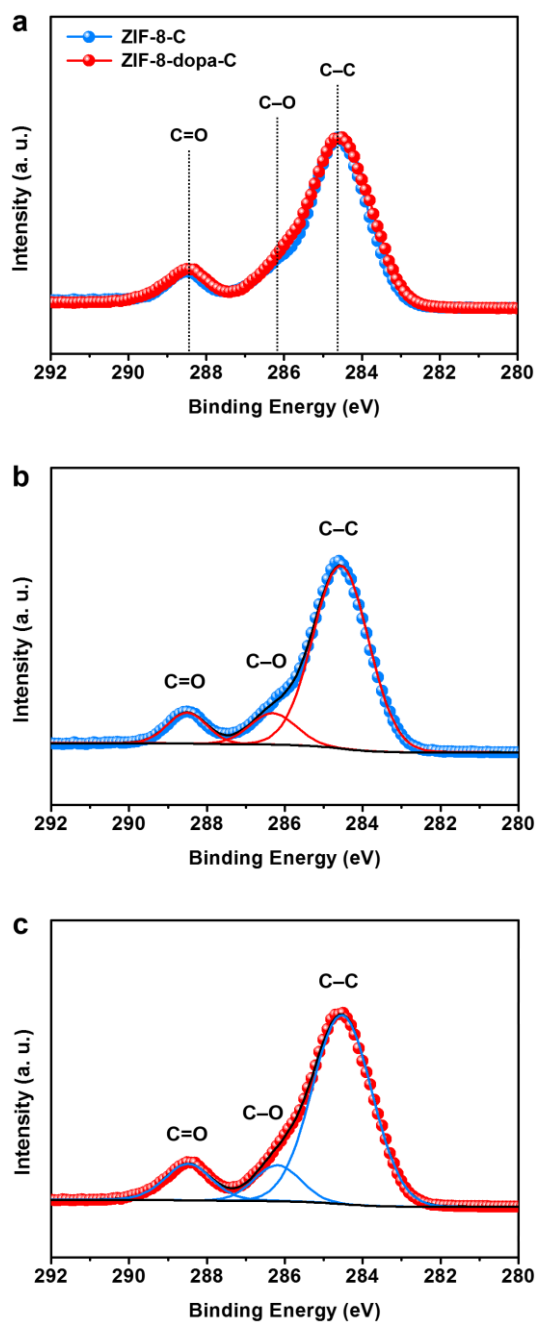


Figure 3.1.10. (a) XPS C 1s spectra of ZIF-8-C and ZIF-8-dopa-C and (b,c)

their fitted results; (b) ZIF-8-C and (c) ZIF-8-dopa-C.

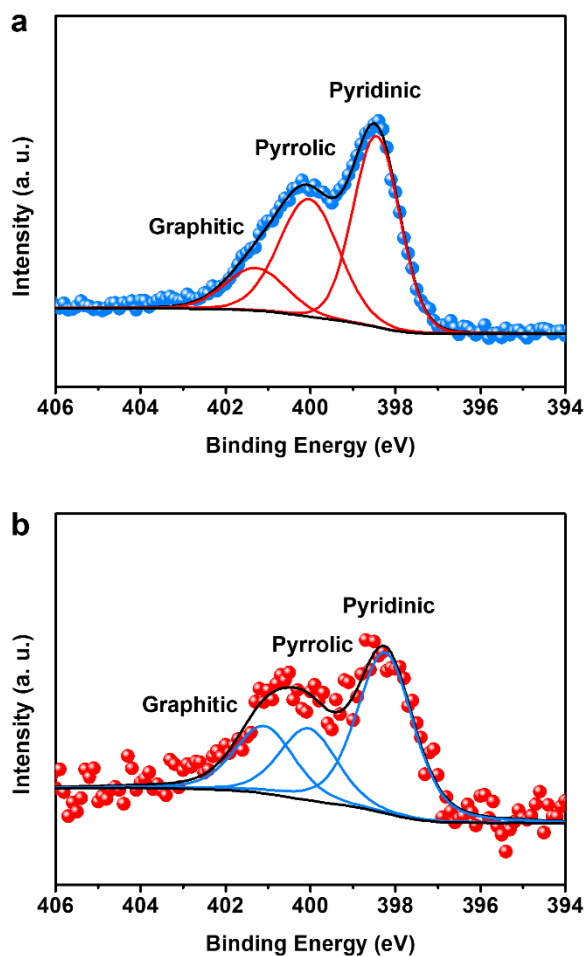


Figure 3.1.11. XPS N 1s spectra of (a) ZIF-8-C and (b) ZIF-8-dopa-C and their fitted results.

Table 3.1.1. Summary of fitting results for XPS (a) carbon 1s and (b) nitrogen 1s spectra of ZIF-8-C and ZIF-8-dopa-C.

(a) Carbon 1s

	Areal Ratio (%)		
	C–C	C–O	C=O
ZIF-8-C	79.12	11.37	9.51
ZIF-8-dopa-C	76.24	11.32	12.44

(b) Nitrogen 1s

	Areal Ratio (%)		
	Pyridinic N	Pyrrolic N	Graphitic N
ZIF-8-C	47.73	38.21	14.06
ZIF-8-dopa-C	53.10	23.61	23.29

Figure 3.1.11. Meanwhile, it was noteworthy that the XAS peak from sp^2 -carbon was larger in ZIF-8-dopa-C than in ZIF-8-C. Given that Zn facilitates graphitization of carbon and that its content is higher in ZIF-8 than in ZIF-8-dopa (because Zn hardly exists in the pristine polydopamine shell), ZIF-8-C was likely to show a larger sp^2 -carbon signal than ZIF-8-dopa-C. Nevertheless, XAS peak at 285.3 eV was larger in the case of ZIF-8-dopa-C. This observation also supports our approach, that introduction of polydopamine shell confines Zn vapor within the ZIF particle for a longer time and thereby increase the influence of Zn during the carbonization (graphitization and pore enlargement).

3.2. Electrochemical performance for triiodide reduction

In order to prepare CEs employing ZIF-8-C or ZIF-8-dopa-C as electrocatalysts, N-doped carbons were sprayed onto fluorine-doped tin oxide (FTO)/glass substrates with the assistance of Nafion binders, and the areal loading of the ZIF-derived N-doped carbons were 0.3 mg/cm². The deposited N-doped carbons were then heat-treated at 500 °C in an Ar-filled tube for 4 h to improve structural and electrical connections between the particles. State-of-the-art platinum CEs were also prepared as control samples by thermal decomposition of H₂PtCl₆ on FTO/glass substrates.⁷² Electrocatalytic

activities of Pt, ZIF-8-C, and ZIF-8-dopa-C CEs were first investigated by cyclic voltammetry (CV) analyses in an acetonitrile electrolyte containing I_3^-/I^- redox couples. From the CV diagrams depicted in Fig. 3.2.1a, two sets of redox peaks could be observed; signals from I_3^-/I_2 and I_3^-/I^- at relatively higher and lower potential regions, respectively.^{73,74} Given that CEs are responsible for the reduction of I_3^- to I^- in DSCs, cathodic peaks located at the lower potentials were chosen for proper comparisons (all of the potentials were calculated with regard to the Ag/AgNO₃ reference electrode). The peak for ZIF-8-C CE was located at -0.337 V, which is a more negative potential when compared with -0.286 V of Pt CE. This indicates that ZIF-8-C has lower electrocatalytic activity than the Pt counterpart. On the other hand, the peak potential of ZIF-8-dopa-C CE was observable at a relatively positive position (-0.273 V) compared to the case of Pt CE, and this clearly demonstrates the superior performance of ZIF-8-dopa-C to that of Pt. The trend in the peak potentials matched well with the peak-to-peak distance of I_3^-/I^- reaction, which were 0.269 , 0.367 , and 0.260 V for Pt, ZIF-8-C, and ZIF-8-dopa-C CEs, respectively.

Moreover, ZIF-8-dopa-C manifested the largest current densities among the three CEs prepared in this study, implying that the amount of I_3^- species being reduced to I^- is the greatest when ZIF-8-dopa-C is used as the

electrocatalyst. Though the large current density of ZIF-8-dopa-C CE compared to Pt counterpart was ascribable to its large surface area originated from the porous structure, it was interesting to observe smaller currents from ZIF-8-C CE. As can be seen from the strong linear correlation between the peak current densities and the square root of scan rates in Figure 3.2.2, electrocatalytic reduction of I_3^- to I^- is governed by mass transfer rate of the reactants and products. Given that the BET surface area of ZIF-8-C was significantly larger than that of ZIF-8-dopa-C, the smaller current densities of ZIF-8-C shows that its large surface area is not being utilized effectively in the electrocatalysis of I_3^-/I^- , due to the hindrance in mass transfer of the triiodide species caused by insufficient pore sizes. This clearly shows that the enlarged pore in ZIF-8-dopa-C increased the overall electrocatalytic performance by effective utilization of its nanostructure and facilitation of mass transfer of the redox species.

Additionally, long-term stability of the ZIF-derived N-doped carbons was investigated. Figures 3.2.1b-d show the CV diagrams of Pt, ZIF-8-C, and ZIF-8-dopa-C measured up to 100 cycles. High durability of ZIF-8-dopa-C was observable from excellent retention of the peak potential, though slight decrease in current density was unavoidable. In contrast, significant drop of electrocatalytic activity was noted in the case of ZIF-8-C. As stated above,

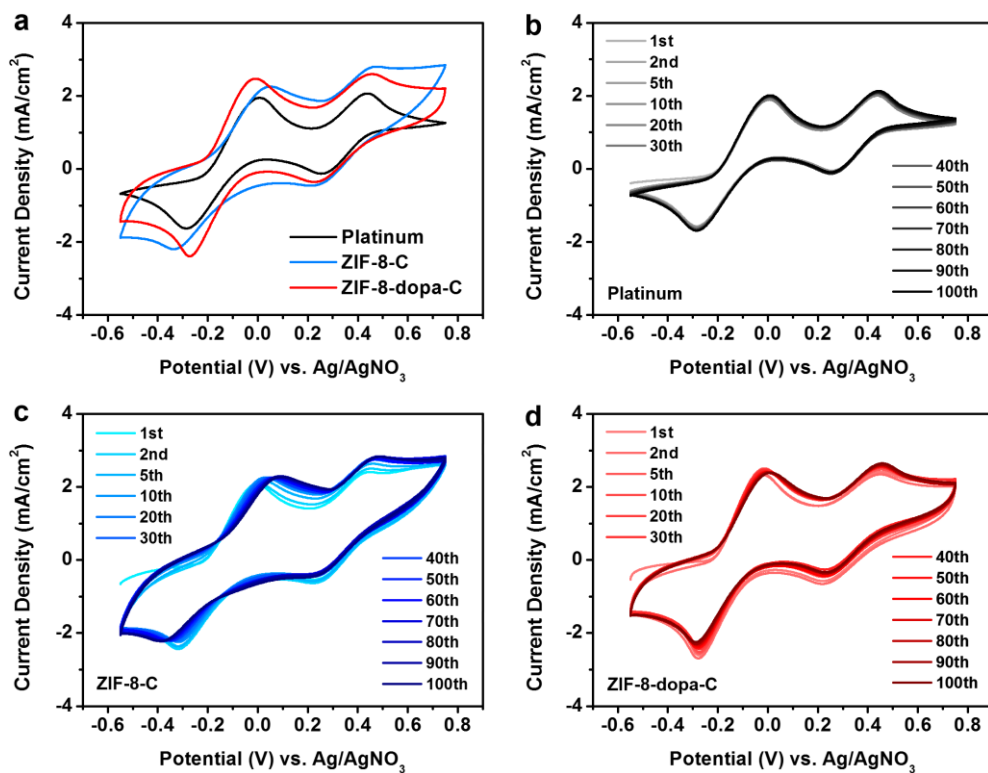


Figure 3.2.1. (a) CV diagrams of platinum, ZIF-8-C, and ZIF-8-dopa-C CE. Data from 10th cycle were depicted for comparisons. (b-d) 100 cycles of CV for (b) platinum, (c) ZIF-8-C, and (d) ZIF-8-dopa-C CE.

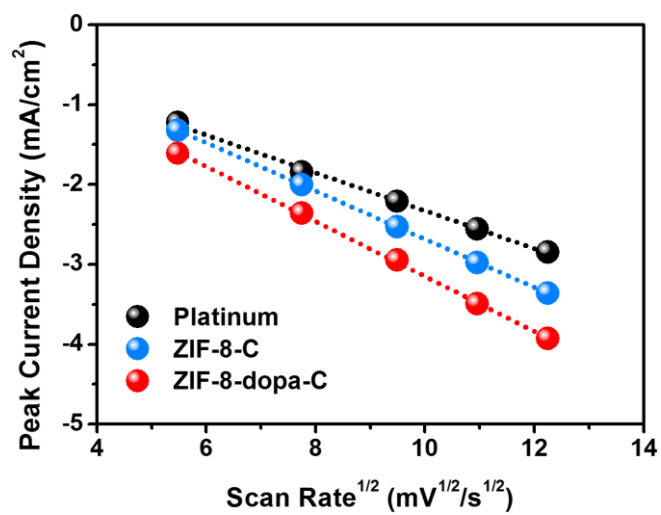


Figure 3.2.2. Peak current densities vs. (scan rate)^{1/2} plots of Pt, ZIF-8-C, and ZIF-8-dopa-C obtained from the I₃⁻/I⁻ peak of the CV data measured at various scan rates (30, 60, 90, 120, 150 mV/s).

ZIF-8-C seems to suffer from poor mass transfer of redox species due to its small-sized pores. In this case, significant amount of accumulated charges in ZIF-8-C CE may not participate in the I_3^- reduction but consequentially degrades the electrode materials. On the other hand, ZIF-8-dopa-C with enlarged pores showed superior characteristics in both electrocatalytic performance and durability, owing to the enhanced mass transfer of redox species that enables them to reach active sites more easily.

For a more accurate comparison on electrocatalytic performances, symmetric cells were prepared by assembling the identical CEs using 50 μm -thick thermoplastic sealants (Surlyn, DuPont) followed by injection of I_3^-/I^- redox electrolyte. Figure 3.2.3a shows the Tafel polarization curves of the symmetric cells employing Pt, ZIF-8-C, or ZIF-8-dopa-C CEs. ZIF-8-dopa-C manifested the largest current densities in all voltage regions, demonstrating the highest electrocatalytic performance of ZIF-8-dopa-C among the three CE materials. Meanwhile, an opposite behavior was observed in ZIF-8-C and Pt CEs depending on the applied voltages. When the voltage was relatively low (kinetic region), Pt showed higher current density than ZIF-8-C. This tendency was reversed in relatively high-voltage region, wherein the number of active sites has larger influence. This implies that Pt has higher catalytic activity but smaller surface area than the case of ZIF-8-

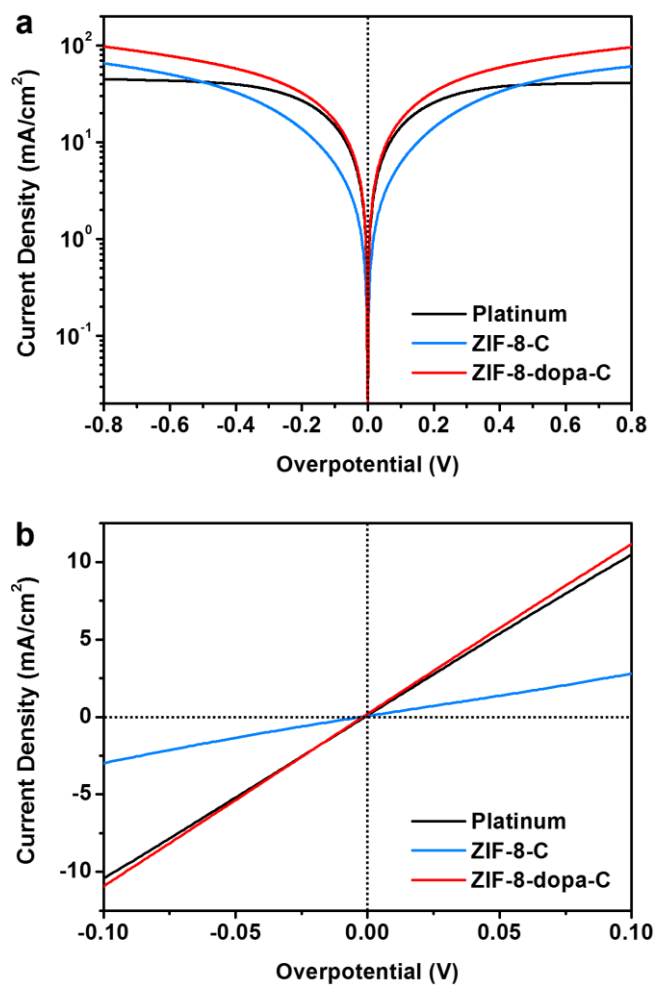


Figure 3.2.3. (a) Tafel polarization curves of symmetric cells employing platinum, ZIF-8-C, or ZIF-8-dopa-C, and (b) polarization curves of the same symmetric cells near zero-voltage region.

C. For a clearer evaluation of the electrocatalytic performances, the trend in exchange current density (J_0) was compared based on the slopes of the polarization curves in the zero-voltage region (Figure 3.2.3b). ZIF-8-dopa-C manifested a larger slope and thus a larger J_0 compared to Pt, from which the superior performance of ZIF-8-dopa-C could be clearly confirmed. ZIF-8-C showed the smallest slope as expected from the CV results and Tafel polarization curves.

3.3. Analyses on kinetics by factors

In order to understand the origin of the high performance of ZIF-8-dopa-C in I_3^-/I^- electrocatalysis, electrochemical impedance spectroscopy (EIS) analyses were carried out using the symmetric cells. Figures 3.3.1a-c show the Nyquist diagrams of the symmetric cells employing Pt, ZIF-8-C, or ZIF-8-dopa-C measured at various temperatures (from 283 to 323 K), respectively. The EIS results were fitted according to the equivalent circuit in Figure 3.3.2,⁷⁵ and the detailed values are displayed in Table 3.3.1 and Figures 3.3.1d and e. It is notable that there were small semicircles at the x-intercept (high-frequency region) of the Nyquist plots in the cases of ZIF-8-C and ZIF-8-dopa-C (see Figure 3.3.3 for magnified plots). These signals were often observed when porous carbons were applied as CE materials, but their origin

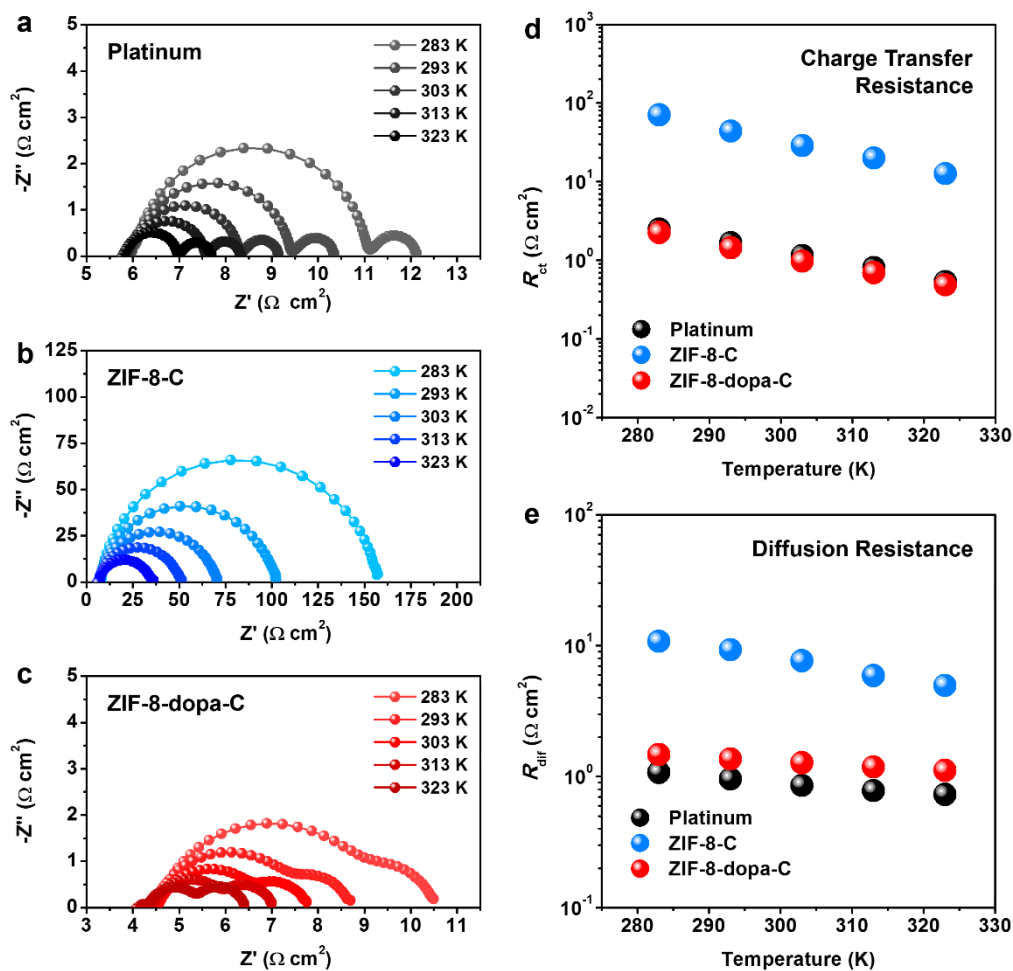


Figure 3.3.1. (a-c) Nyquist plots of the symmetric cells employing (a) platinum, (b) ZIF-8-C, and (c) ZIF-8-dopa-C measured at diverse temperatures. (d,e) Parameters obtained by fitting the EIS data; (d) charge transfer resistance and (e) diffusion resistance.

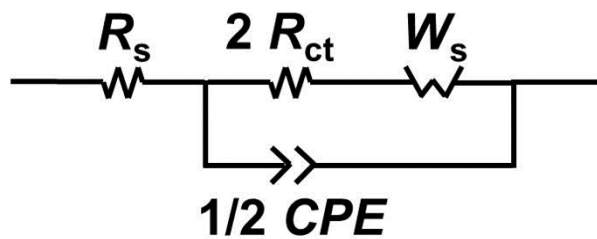


Figure 3.3.2. Equivalent circuit for EIS analyses of symmetric cells.

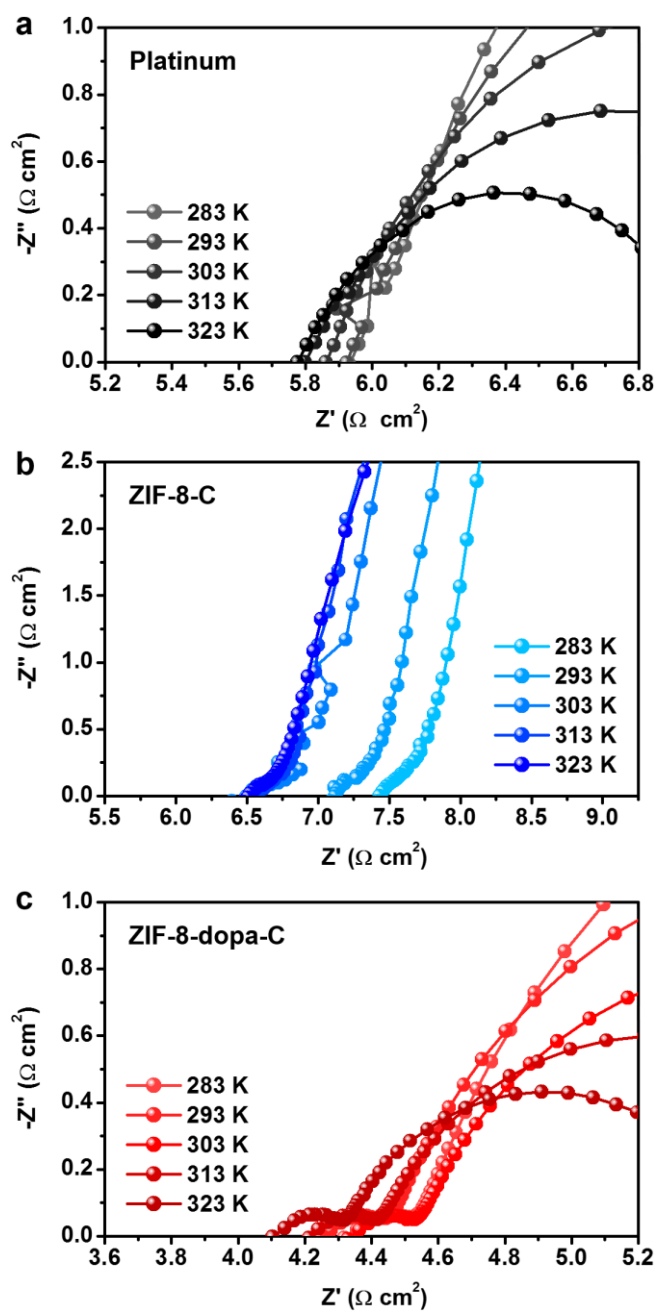


Figure 3.3.3. Enlarged Nyquist plots of the symmetric cells employing (a) Pt, (b) ZIF-8-C, and (c) ZIF-8-dopa-C CE near the high-frequency region.

Table 3.3.1. Summary of fitting results for EIS spectra of the symmetric cells employing (a) platinum, (b) ZIF-8-C, and (c) ZIF-8-dopa-C electrodes.

(a) Platinum

Temperature	R_s ($\Omega \text{ cm}^2$)	R_{ct} ($\Omega \text{ cm}^2$)	R_{dif} ($\Omega \text{ cm}^2$)
283 K	5.961	2.479	1.076
293 K	5.924	1.672	0.9594
303 K	5.861	1.153	0.8575
313 K	5.830	0.8061	0.7811
323 K	5.776	0.5361	0.7301

(b) ZIF-8-C

Temperature	R_s ($\Omega \text{ cm}^2$)	R_{ct} ($\Omega \text{ cm}^2$)	R_{dif} ($\Omega \text{ cm}^2$)
283 K	7.432	70.60	10.75
293 K	7.119	43.77	9.303
303 K	6.503	28.75	7.647
313 K	6.562	19.95	5.898
323 K	6.511	12.66	4.964

(c) ZIF-8-dopa-C

Temperature	R_s ($\Omega \text{ cm}^2$)	R_{ct} ($\Omega \text{ cm}^2$)	R_{dif} ($\Omega \text{ cm}^2$)
283 K	4.326	2.252	1.475
293 K	4.258	1.441	1.367
303 K	4.340	0.9747	1.276
313 K	4.218	0.6978	1.186
323 K	4.107	0.4857	1.113

is still controversial; these semicircles are expected to be related to the Nernst diffusion of iodide species within the pores in the carbon^{76,77} or the response from the basal plane of carbon.¹⁷ Nonetheless, these semicircles were not taken into account in this study, because they are known to be of minor importance to the electrocatalytic performances of CEs and also those of DSCs.

Series resistance (R_s), which shows the overall ohmic resistance of the symmetric cell, is strongly dependent on the electrode-electrode distance in addition to the conductivities of electrocatalysts.⁶ For this reason, the difference in R_s values was not considered important, except for that between the cells employing ZIF-8-C and ZIF-8-dopa-C. R_s of the symmetric cell employing ZIF-8-dopa-C was significantly smaller than the ZIF-8-C-based cell. This was attributable to the difference in their electrical properties; porous carbon materials with larger pore sizes often have superior conductivity due to the thicker interconnecting channels. In addition, it was verified from the XAS analysis (Figure 3.1.9a) that the degree of sp^2 characteristic was larger in ZIF-8-dopa-C compared to the case of ZIF-8-C, and this seems to be another reason for the superior electrical property of ZIF-8-dopa-C.

Charge transfer resistance (R_{ct}) values of the prepared CEs were

compared in order to investigate the charge transfer kinetics at the electrode/electrolyte interface. R_{ct} was the smallest in ZIF-8-dopa-C at all temperatures within the measurement range, followed by Pt and ZIF-8-C. This result is in line with the previous observations from the CV diagrams and the polarization curves of the symmetric cells, demonstrating the superior electrocatalytic performance of ZIF-8-dopa-C CEs. Mass transfer characteristics of I_3^-/I^- in the cells employing Pt, ZIF-8-C, or ZIF-8-dopa-C CEs were then investigated by comparing diffusion resistance (R_{dif}) values. Among three CEs, Pt showed the smallest R_{dif} , and this could be understood as the result of its non-porous structure. Meanwhile, ZIF-8-C and ZIF-8-dopa-C manifested substantial difference in mass transfer of I_3^-/I^- . As previously mentioned, the length of I_3^- is around 1 nm and is thereby unlikely to travel through the pores in microporous materials, such as ZIF-8-C. On the other hand, mass transfer of I_3^- in ZIF-8-dopa-C with enlarged pores was significantly enhanced from the case of ZIF-8-C, as can be clearly seen from the smaller R_{dif} values by a degree of order.

Additionally, capacitance retention measurements were carried out for ZIF-8-C and ZIF-8-dopa-C in aqueous solution containing 1.0 M of NaCl or NaClO₄ in order to elucidate the effect of different pore sizes on mass transfer properties of the chemical species within the electrolyte. The ionic radii of

Na^+ and Cl^- are known as 102 pm and 181 pm, respectively, and that of ClO_4^- is known to be around 240 pm.⁷⁸ Meanwhile, hydrated radius of Na^+ is 358 pm, while those of Cl^- and ClO_4^- are 332 and 338 pm, respectively.⁷⁹ The potential window for the capacitance measurement was 0.0 to 0.8 V vs. normal hydrogen electrode (NHE), wherein adsorption and desorption of anions on the electrode surface are responsible for the capacitive currents. Figures 3.3.4 and 3.3.5 show the CV diagrams of the ZIF-derived N-doped carbons in NaCl and NaClO₄ electrolytes, respectively. From the specific capacitances calculated from the area of the CV data, the capacity retentions were obtained and summarized in Figure 3.3.6. The capacitances of ZIF-8-C was around two times larger than that of ZIF-8-dopa-C under slow scan rates, and this observation matched well with the difference in BET surface areas. On the other hand, the retention of capacitance was superior in ZIF-8-dopa-C when compared with that of ZIF-8-C, indicating that the mass transfer limitation is less severe when ZIF-8-dopa-C is used as the CE material. This enhancement is attributable to the enlarged pore size in ZIF-8-dopa-C, which resulted from the incorporation of polydopamine shell on the surface of ZIF-8 prior to the thermal carbonization. Moreover, since I_3^- is significantly larger than Cl^- and ClO_4^- , it could be concluded that the influence of different pore sizes of ZIF-8-C and ZIF-8-dopa-C would be more critical to the mass

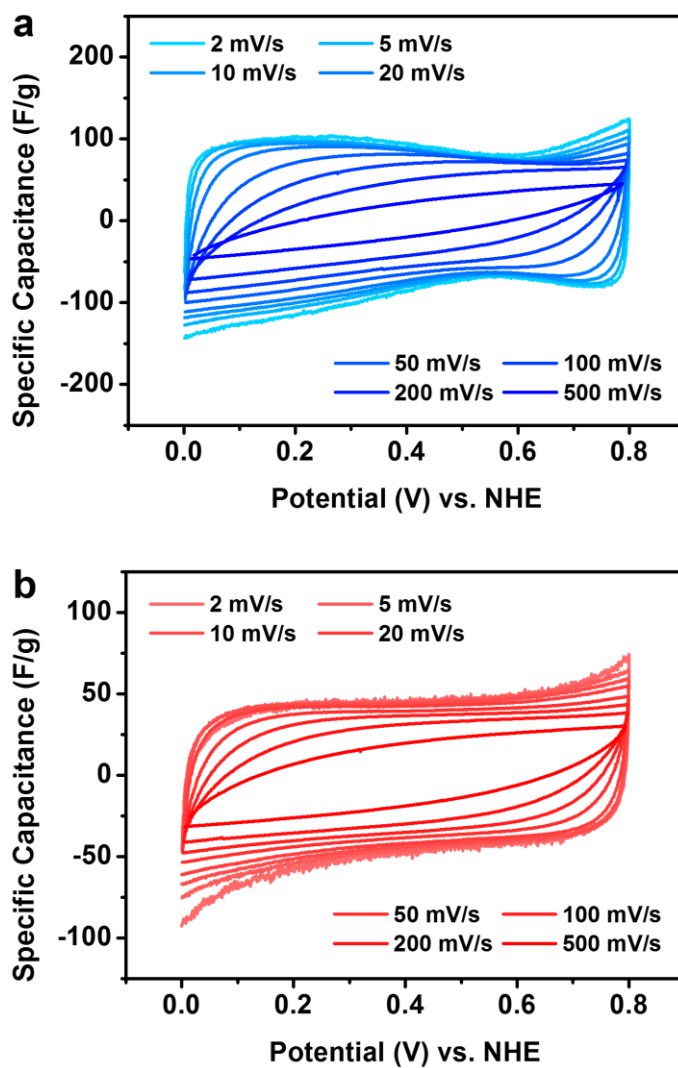


Figure 3.3.4. CV diagrams showing the specific capacitance vs. potential plots for (a) ZIF-8-C and (b) ZIF-8-dopa-C measured at diverse scan rates using 1.0 M NaCl electrolyte.

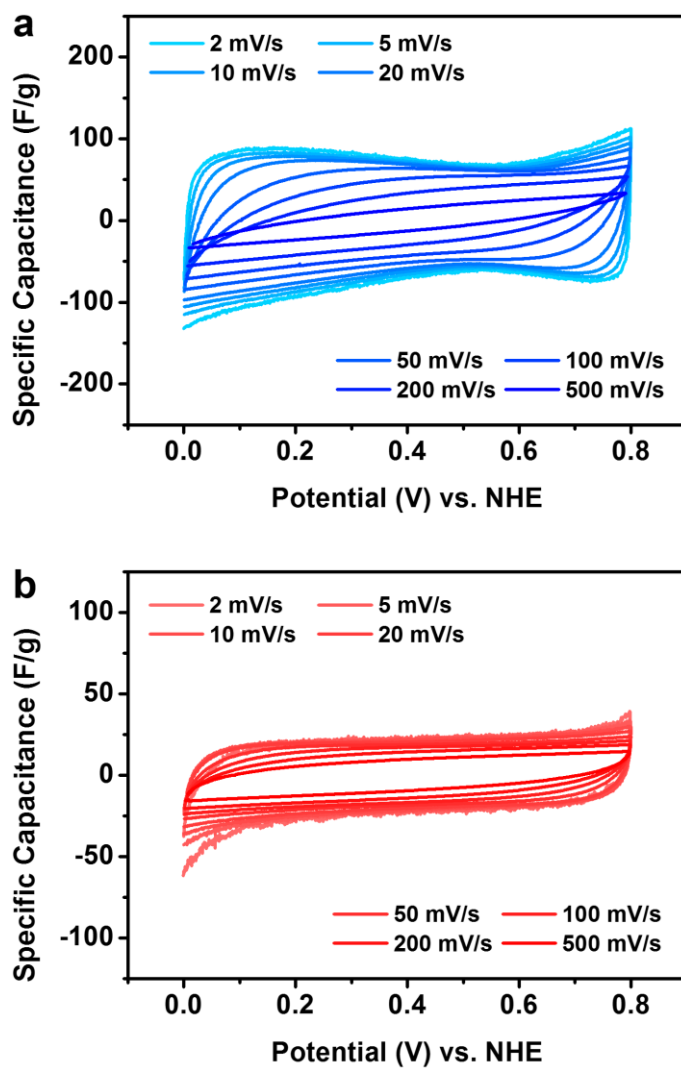


Figure 3.3.5. CV diagrams showing the specific capacitance vs. potential plots for (a) ZIF-8-C and (b) ZIF-8-dopa-C measured at diverse scan rates using 1.0 M NaClO₄ electrolyte.

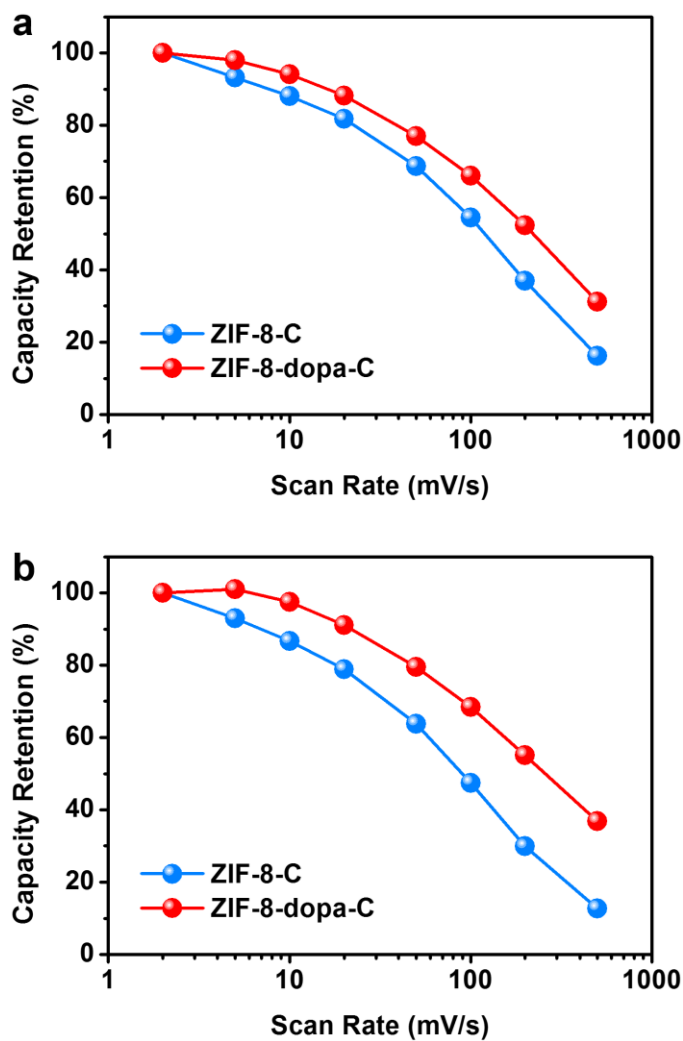


Figure 3.3.6. Capacity retentions of ZIF-8-C and ZIF-8-dopa-C for the cases of (a) 1.0 M NaCl and (b) 1.0 M NaClO₄ electrolytes.

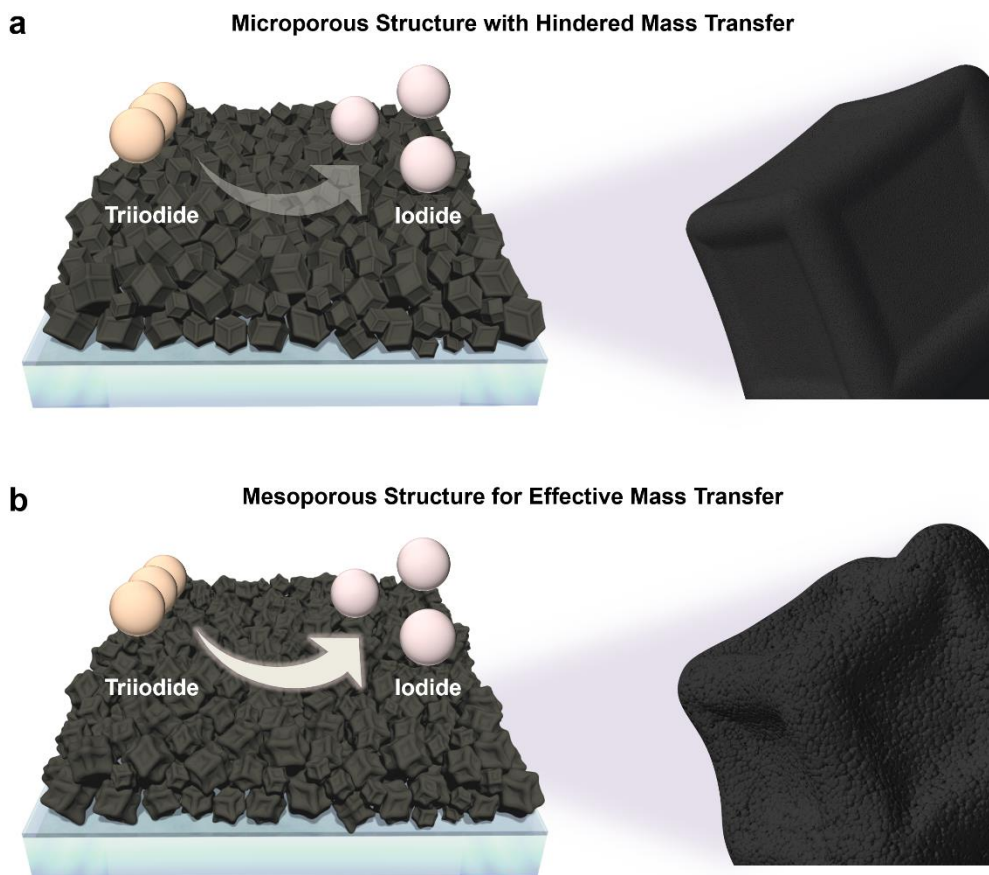


Figure 3.3.7. Schematic illustration of electrocatalytic reduction of triiodide at the surface of (a) microporous ZIF-8-C and (b) mesoporous ZIF-8-dopa-C.

transfer property of I_3^-/I^- redox species.

Meanwhile, it was noteworthy that ZIF-8-dopa-C manifested similar capacitance retention behaviors in both NaCl and NaClO₄ solutions, and this was ascribable to the comparable hydrated radii of Cl^- and ClO_4^- ; the difference is less than 2%. On the other hand, capacity retention of ZIF-8-C was significantly lower in NaClO₄ solution when compared with that for the NaCl electrolyte. It was previously reported that the degree of hydration decreases when ions are spatially confined.⁸⁰ In the same manner, if the concentration of ions is locally too high, overlap between the water molecules may occur, leading to a drop in the number of water molecules participating in the hydration. When positive potential is applied to the ZIF-derived N-doped carbon electrodes, as in the case of the capacitance retention measurements, the number of anions within the pores increases. If the anions get overcrowded in the pores, the ions will then become incompletely hydrated, and the effective sizes of ions will rather depend on the original size of ions (i.e. ionic radius). Considering that Cl^- and ClO_4^- have significantly different ionic radii, imperfect hydration of the anions are likely to cause a large difference in the actual size of ions, and this explains the gap in the capacity retention of ZIF-8-C. In this viewpoint, the inferior capacity retention of ZIF-8-C in NaClO₄ electrolyte can be understood as the

consequence of small pore sizes that does not provide sufficient spaces for complete hydration of ions. These observations clearly demonstrate that the transport of chemical species that are larger than few angstroms are strongly hindered by the small pores sizes. Together with the smaller R_{dif} of ZIF-8-dopa-C compared to the case of ZIF-8-C, the capacity retention measurement results clearly verify that the enhanced electrocatalytic performances are ascribable to the promoted mass transfer, which is originated from the enlarged pore sizes. Figure 3.3.7 shows the schematic illustrations of ZIF-8-C and ZIF-8-dopa-C CEs with significantly different performance in reducing I_3^- into three I^- , which is attributable to the dissimilar pore sizes.

3.4. Comparisons of intrinsic activities

EIS analyses of the symmetric cells reveal that R_{ct} of Pt and ZIF-8-dopa-C are within a comparable range. Given that ZIF-8-dopa-C has a porous structure with large surface area, similar R_{ct} values are ascribable to the large number of active sites of the ZIF-derived carbon and demonstrates the importance of proper nano-architecturing. Meanwhile, in order to further understand the different intrinsic activities of Pt, ZIF-8-C, and ZIF-8-dopa-C, activation energy (E_a) for the electrocatalysis of I_3^-/I^- was calculated. It is well known that J_0 and R_{ct} have the following relationship:^{75,81}

$$J_0 = RT/nFR_{ct} \quad (1)$$

where R is the gas constant, T is the temperature, F is the Faraday constant, and n is the number of electrons that are transferred during the electrochemical reduction of I_3^- to three I^- . Based on the obtained J_0 value, E_a was calculated by using the following Arrhenius equation:^{60,82}

$$J_0 = I_0 e^{-E_a/RT} \quad (2)$$

where I_0 is the exchange current density at infinite T . By plotting the $\log J_0$ values against $1000/T$ (see Table 3.4.1 and Figure 3.4.1), E_a for Pt, ZIF-8-C, and ZIF-8-dopa-C were approximated as 31.30, 34.60, and 31.36 kJ/mol, respectively. Pt showed the smallest E_a , while those of ZIF-8-C and ZIF-8-dopa-C were somewhat larger. As previously mentioned, higher nitrogen-content in the N-doped carbon often leads to a superior catalytic performance by providing active sites with higher intrinsic activity. Meanwhile, E_a of ZIF-8-dopa-C was smaller than that of ZIF-8-C though the N-content of ZIF-8-C was higher. It is widely known that the electrochemical reduction of I_3^- to I^- takes place through the following three-step reactions:

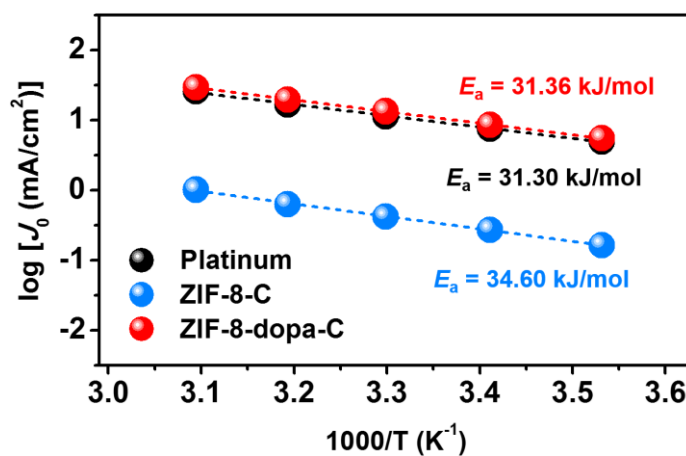


Figure 3.4.1. Arrhenius plot of the symmetric cells constructed by calculation of exchange current densities using the geometric area-normalized charge transfer resistance values.

Table 3.4.1. Exchange current densities in the symmetric cells employing platinum, ZIF-8-C, or ZIF-8-dopa-C at diverse temperatures and the corresponding activation energies calculated using Arrhenius equation.

	J_0 (mA/cm ²)					Slope (1/K)	E_a (kJ/mol)
	283 K	293 K	303 K	313 K	323 K		
Platinum	4.920	7.552	11.33	16.74	25.97	−1.637	31.30
ZIF-8-C	0.1728	0.2886	0.4543	0.6763	1.100	−1.809	34.60
ZIF-8-dopa-C	5.417	8.765	13.40	19.33	28.67	−1.640	31.36



where * stands for the free active site on the electrode surface. The first step is known to be fast and in equilibrium, and the other two steps are in charge of the overall rate of I_3^-/I^- redox reactions.⁷³ In general, activities of electrocatalysts are strongly dependent on the binding energy of the reaction intermediates on the catalyst surface.^{83,84} According to the reports by Hou et al.⁸² and Wang et al.,⁸⁵ electrocatalytic activities of CEs are governed by the adsorption energy of I atom on the surface, with the optimum at the intermediate binding strength that is not too weak or strong. In this aspect of view, the binding energy of I on ZIF-8-dopa-C seems to be located near the optimum and catalyze I_3^- reduction with high intrinsic activity, though E_a cannot be directly correlated to the adsorption energy. Based on these results, it could be concluded that high overall performance of ZIF-8-dopa-C is originated not only from the enhanced accessibility originated from enhanced mass transfer of I_3^-/I^- redox couples by enlarged pore sizes but also high catalytic activities per available sites.

As mentioned in the former paragraphs, higher N-content in

carbonaceous electrocatalysts often leads to superior catalytic performances by providing certain sites with higher intrinsic activity. Meanwhile, E_a of ZIF-8-dopa-C was smaller than that of ZIF-8-C though the N-content of ZIF-8-C was higher. In order to elucidate this unexpected observation, Raman analyses were additionally carried out, whose results are displayed in Figure 3.4.2. The peaks located at the wavenumber of around 1350 and 1590 cm^{-1} were assigned as defective carbon (D) and graphitic carbon (G) peaks,⁸⁶ respectively. The signals from sp^3 carbons known to appear at approximately 1200 and 1500 cm^{-1} were not taken account, because they were hardly distinguishable from the Raman spectra.^{87,88} The D/G ratios based on the peak intensities were 0.921 for ZIF-8-C and 0.949 for ZIF-8-dopa-C, and the D peak of ZIF-8-C was broader than that of ZIF-8-dopa-C. Since there was no notable difference in the G peaks, it could be concluded that the defect density is higher in ZIF-8-dopa-C than in ZIF-8-C. Given that defect sites are more active than ordered surfaces in carbonaceous electrocatalysts for triiodide reduction,^{16,18} larger number of defects in ZIF-8-dopa-C was expected as one of the reasons for the superior catalytic activity.

Regarding the different intrinsic performances, it was also notable that there was significant difference in the portion of N species in ZIF-8-C and ZIF-8-dopa-C. In various electrochemical reactions, binding energy of a

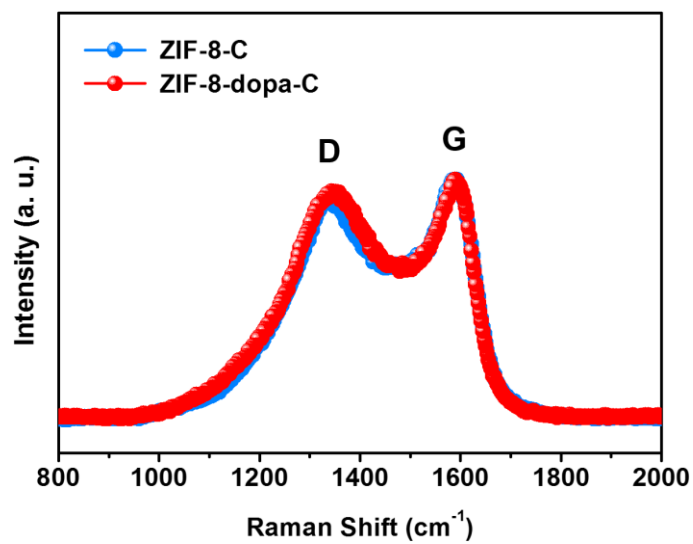


Figure 3.4.2. Raman spectra of (a) ZIF-8-C and (b) ZIF-8-dopa-C.

reactant is strongly dependent on the types of the N species, which tailors the electronic structure of the adjacent carbon atoms that usually serve as active sites.^{70,71,77} In XPS N 1s data of ZIF-8-C and ZIF-8-dopa-C (in Figure 3.1.11), the portions of pyridinic N and graphitic N were higher in ZIF-8-dopa-C while its pyrrolic N content was lower than that in ZIF-8-C. Since the XPS results of ZIF-8-dopa-C mainly show the responses from polydopamine-derived shell parts, the different N species cannot serve as the main origin of the different catalytic activity. Nevertheless, there is a possibility that pyridinic and graphitic N engenders the formation of catalytic sites with a higher activity (i.e. a more favorable I adsorption energy) than the case of pyrrolic N, and superior performances of N-doped carbon with high component ratios of pyridinic and graphitic N have been reported.^{77,89} Presumably, further analyses on the different types of N (either by experimental or computational methods) would enable deeper understandings on the N-doped carbon catalysts for triiodide reduction and provide important guidelines for the catalyst design.

3.5. Applications in mesoscopic solar cells

Finally, ZIF-derived N-doped carbons were applied as electrocatalytic CEs of DSCs employing I_3^-/I^- redox electrolyte. Mesoscopic photoelectrodes were

prepared by doctor-blading and thermal sintering of the colloidal TiO_2 nanoparticles on FTO/glass substrates followed by adsorption of N719 dyes on the surface. The cell assembly was carried out by using the thermoplastic sealants, and the electrolytes were then injected into the cells. Figure 3.5.1a shows the photocurrent density (J)–voltage (V) characteristics of DSCs employing Pt, ZIF-8-C, or ZIF-8-dopa-C CEs, and the detailed photovoltaic parameters are summarized in Table 3.5.1. Since all of the photoelectrodes for the DSCs were prepared by identical procedures, open-circuit voltage (V_{oc}) and short-circuit photocurrent density (J_{sc}) values were not considered as important indicators. V_{oc} and J_{sc} mainly show the light harvesting and charge collection characteristic of photoelectrodes, and they do not often show meaningful behaviors with regard to the performances of CEs. On the other hand, fill factors (FF s), which is strongly influenced by the overpotentials in I_3^- reduction in CEs, showed notable differences. It was previously observed from the polarization curves of the symmetric cells (in Figure 3.2.3b) that the overpotential in the electrocatalysis of I_3^-/I^- was smallest for ZIF-8-dopa-C followed by Pt and ZIF-8-C. The trend in FF values were also in the order of ZIF-8-dopa-C > Pt > ZIF-8-C. As a result, the power conversion efficiencies of DSCs employing ZIF-8-dopa-C CEs ($8.95 \pm 0.10\%$) was significantly higher than those with ZIF-8-C CEs ($8.26 \pm 0.10\%$)

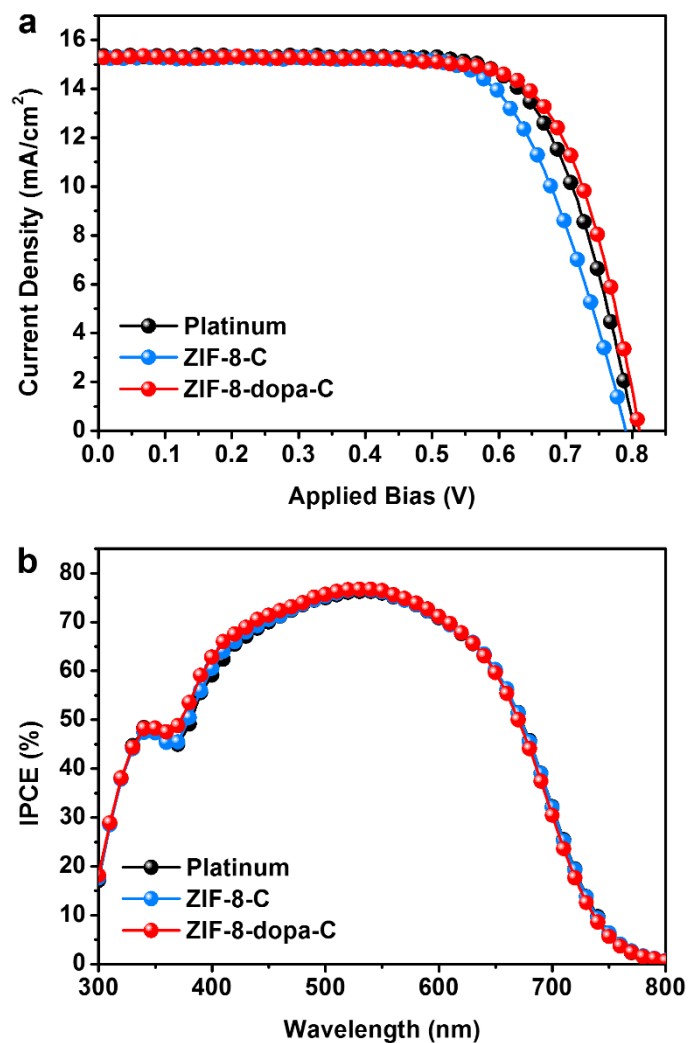


Figure 3.5.1. (a) J - V curves of DSCs employing platinum, ZIF-8-C, or ZIF-8-dopa-C CEs measured under standard 1 sun illumination (AM 1.5G condition). (b) IPCE spectra of the same DSCs.

Table 3.5.1. Fill factors and power conversion efficiencies of DSCs employing carbon-based CEs reported in previous publications and from our experiment. The comparison on the performances is limited to the N719 dye- and I_3^-/I^- redox electrolyte-based cells for proper evaluations.

Counter Electrode Material	Fill Factor (%)	Efficiency (%)	Reference
Carbon Black	68.5	9.10	(1)
Carbon Black	65.6	7.20	(2)
Carbon Black	71.3	8.35	(3)
Carbon Black + Graphite	71.2	6.67	(4)
Carbon Nanofiber	70	7.00	(5)
Single-Walled Carbon Nanotube	74	7.81	(6)
Single-Walled Carbon Nanotube	58.7	8.31	(7)
Multi-Walled Carbon Nanotube	64	7.67	(8)
Multi-Walled Carbon Nanotube	71	7.63	(6)
Reduced Graphene Oxide	72	7.19	(9)
N- and P-doped Graphene	72	8.57	(10)
Graphite Nanoball	67	7.88	(11)
Ordered Mesoporous Carbon	65	7.50	(12)
Carbonized ZIF-8	68	7.32	(13)
ZIF-8-dopa-C	72.8	9.03	our work

or Pt CEs ($8.76 \pm 0.13\%$), with the champion performance of 9.03%. This value was among the state-of-the-art results from the DSCs with carbon-based electrocatalytic CEs, as can be seen from the comparisons with the values reported in previous publications displayed in Table 3.5.1. Figure 3.5.1b shows the incident photon-to-current efficiency (IPCE) of the DSCs employing Pt or ZIF-derived N-doped carbons, from which it could be verified that the spectral responses are comparable for the DSCs regardless of the CEs. This matched well with the $J-V$ results, and it also clearly showed that the difference in the photovoltaic performances were originated from the diverse electrocatalytic performances of the CEs and not from the photoelectrodes, which were identical in all of the prepared DSCs.

Additionally, $J-V$ measurements were carried out on DSCs employing the ZIF-derived N-doped carbon CEs using a cobalt bipyridine ($[\text{Co}(\text{bpy})_3]^{3+/2+}$) redox electrolyte, in order to investigate the performances of the porosity-tailored carbons when larger-sized redox species are utilized. As can be seen from Table 3.5.2 and Figure 3.5.2, ZIF-8-dopa-C in place of Pt induced a dramatic drop in performance, and the performance was even lower when ZIF-8-C was used in the CE. These results were attributable to the poorer mass transfer of bulky $[\text{Co}(\text{bpy})_3]^{3+/2+}$ redox couples when compared with I_3^-/I^- species, indicating that further increase in pore sizes are essential

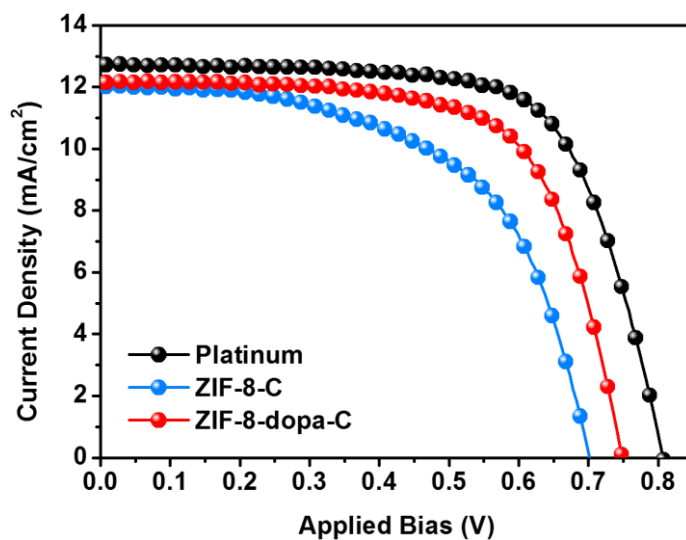


Figure 3.5.2. J - V curves of DSCs employing $[\text{Co}(\text{bpy})_3]^{3+/2+}$ redox electrolyte and platinum, ZIF-8-C, and ZIF-8-dopa-C CE measured under standard 1 sun illumination (AM 1.5G condition).

Table 3.5.2. Summary of J – V characteristics for DSCs employing $[\text{Co}(\text{bpy})_3]^{3+/2+}$ redox electrolyte and platinum, ZIF-8-C, and ZIF-8-dopa-C CEs.

	V_{oc} (V)	J_{sc} (mA/cm ²)	FF (%)	η (%)
Platinum	0.807	12.76	68.7	7.07
ZIF-8-C	0.701	12.01	57.5	4.84
ZIF-8-dopa-C	0.749	12.17	67.2	6.12

for chemical species that are significantly larger than I_3^- . This observation clearly demonstrates the effectiveness of the approach in this study, and also emphasizes the importance of tailoring the pore sizes in accordance with the chemical species taking part in the targeted reactions.

Chapter 4. Conclusions

In this study, porous N-doped carbons were prepared by thermal carbonization of ZIF-8 and were applied as electrocatalysts in DSCs. In order to resolve the significant mass transfer resistance of I_3^-/I^- redox electrolyte in ZIF-8-derived carbon materials, the pore sizes were increased by incorporation of polydopamine shell on the surface of ZIF-8 prior to the thermal carbonization. This additional layer elongated the dwelling time of Zn within ZIF-8 and increased the size of pores in the resulting carbon materials. The N-doped carbon with augmented pore sizes manifested significantly enhanced electrocatalytic performances, which led to a superior energy conversion efficiency to the case of state-of-the-art Pt counterpart, with the champion value exceeding 9%. Considering the reliability and robustness of the methods used in this study, these results and observations are even more promising. Moreover, since the approaches in this study give simple route to control the pore sizes of carbonized MOFs, which are useful in various catalytic applications, the investigations performed here are anticipated to provide important insights and profound understandings on the design of MOF-based functional materials.

Acknowledgement

This thesis was reproduced from Ref. 91.

References

- 1 B. O'Regan and M. Grätzel, *Nature*, 1991, **353**, 737-740.
- 2 A. Yella, H.-W. Lee, H. N. Tsao, C. Yi, A. K. Chandiran, M. K. Nazeeruddin, E. W.-G. Diau, C.-Y. Yeh, S. M. Zakeeruddin and M. Grätzel, *Science*, 2011, **334**, 629-634.
- 3 K. Kakiage, Y. Aoyama, T. Yano, K. Oya, J.-i. Fujisawa and M. Hanaya, *Chem. Commun.*, 2015, **51**, 15894-15897.
- 4 M. Y. Jin, B.-M. Kim, H. S. Jung, J.-H. Park, D.-H. Roh, D. G. Nam, T.-H. Kwon, D. H. Ryu, *Adv. Funct. Mater.*, 2016, **26**, 6876-6887.
- 5 M. Freitag, J. Teuscher, Y. Saygili, X. Zhang, F. Giordano, P. Liska, J. Hua, S. M. Zakeeruddin, J.-E. Moser, M. Grätzel and A. Hagfeldt, *Nat. Photonics*, 2017, **11**, 372-378.
- 6 J. S. Kang, H. Choi, J. Kim, H. Park, J.-Y. Kim, J.-W. Choi, S.-H. Yu, K. J. Lee, Y. S. Kang, S. H. Park, Y.-H. Cho, J.-H. Yum, D. C. Dunand, H. Choe and Y.-E. Sung, *Small*, 2017, **13**, 1701458.
- 7 M. Grätzel, *Nature*, 2001, **414**, 338-344.
- 8 M. Grätzel, *Inorg. Chem.*, 2005, **44**, 6841-6851.
- 9 A. Hagfeldt, G. Boschloo, L. Sun, L. Kloo and H. Pettersson, *Chem. Rev.*, 2010, **110**, 6595.
- 10 M. Wu and T. Ma, *ChemSusChem*, 2012, **5**, 1343-1357.
- 11 S. Thomas, T. G. Deepak, G. S. Anjusree, T. A. Arun, S. V. Nair and A. S. Nair, *J. Mater. Chem. A*, 2014, **2**, 4474-4490.

- 12 Z. Yajing, H. Guo, H. Zheng, Y.-n. Lin, C. Gao, Q. Han and M. Wu, *Nano Energy*, 2016, **21**, 1-18.
- 13 J. Wu, Z. Lan, J. Lin, M. Huang, Y. Huang, L. Fan, G. Luo, Y. Lin, Y. Xie and Y. Wei, *Chem. Soc. Rev.*, 2017, **46**, 5975-6023.
- 14 A. Kay and M. Grätzel, *Sol. Energy Mater. Sol. Cells*, 1996, **44**, 99-117.
- 15 T. N. Murakami, S. Ito, Q. Wang, M. K. Nazeeruddin, T. Bessho, I. Cesar, P. Liska, R. Humphry-Baker, P. Comte, P. Péchy and M. Grätzel, *J. Electrochem. Soc.*, 2006, **153**, A255-A2261.
- 16 M. Kouhnavard, N. A. Ludin, B. V. Ghaffari, K. Sopian and S. Ikeda, *ChemSusChem*, 2015, **8**, 1510-1533.
- 17 M. J. Ju, I.-Y. Jeon, H. M. Kim, J. I. Choi, S.-M. Jung, J.-M. Seo, I. T. Choi, S. H. Kang, H. S. Kim, M. J. Noh, J.-J. Lee, H. Y. Jeong, H. K. Kim, Y.-H. Kim and J.-B. Baek, *Sci. Adv.*, 2016, **56**, e1501459.
- 18 M. Chen and L.-L. Shao, *Chem. Eng. J.*, 2016, **304**, 629-645.
- 19 Z. Li, B. Ye, X. Hu, X. Ma, X. Zhang and Y. Deng, *Electrochem. Commun.*, 2009, **11**, 1768-1771.
- 20 Q. Tai, B. Chen, F. Guo, S. Xu, H. Hu, B. Sebo and X.-Z. Zhao, *ACS Nano*, 2011, **5**, 3795-3799.
- 21 H. Ellis, N. Vlachopoulos, L. Häggman, C. Perruchot, M. Jouini, G. Boschloo and A. Hagfeldt, *Electrochim. Acta*, 2013, **107**, 45-51.
- 22 S. H. Park, O.-H. Kim, J. S. Kang, K. J. Lee, J.-W. Choi, Y.-H. Cho and Y.-E. Sung, *Electrochim. Acta.*, 2014, **137**, 661-667.
- 23 M. Wang, A. M. Anghel, B. Marsan, N.-L. C. Ha, N. Pootrakulchote, S. M. Zakeeruddin and M. Grätzel, *J. Am. Chem. Soc.*, 2009, **131**, 15976-15977.
- 24 W. S. Chi, J. W. Han, S. Yang, D. K. Rho, H. Lee and J. H. Kim, *Chem. Commun.*, 2012, **48**, 9501-9503.

- 25 M. Wu, X. Lin, Y. Wang, L. Wang, W. Guo, D. Qi, X. Peng, A. Hagfeldt, M. Grätzel and T. Ma, *J. Am. Chem. Soc.*, 2012, **134**, 3419-3428.
- 26 F. Gong, H. Wang, X. Xu, G. Zhou and Z.-S. Wang, *J. Am. Chem. Soc.*, 2012, **134**, 10953-10958.
- 27 M. Wu, Y.-n. Lin, H. Guo, K. Wu and X. Lin, *Chem. Commun.*, 2014, **50**, 7625-7627.
- 28 J. S. Kang, J. Kim, M. J. Lee, Y. J. Son, J. Jeong, D. Y. Chung, A. Lim, H. Choe, H. S. Park and Y.-E. Sung, *Nanoscale*, 2017, **9**, 5413-5424.
- 29 W. Hou, Y. Xiao and G. Han, *Angew. Chem. Int. Ed.*, 2017, **56**, 9146-9150.
- 30 J. S. Kang, J.-Y. Kim, J. Yoon, J. Kim, J. Yang, D. Y. Chung, M.-c. Kim, H. Jeong, Y. J. Son, B. G. Kim, J. Jeong, T. Hyeon, M. Choi, M. J. Ko and Y.-E. Sung, *Adv. Energy Mater.*, 2018, **8**, 1703114.
- 31 Z. Khan, S. Park, S. M. Hwang, J. Yang, Y. Lee, H.-K. Song, Y. Kim and H. Ko, *NPG Asia Mater.*, 2016, **8**, e294.
- 32 S.-K. Park, D. Y. Chung, D. Ko, Y.-E. Sung and Y. Piao, *J. Mater. Chem. A*, 2016, **4**, 12720-12725.
- 33 Z. Khan, B. Senthilkumar, S. O. Park, S. Park, J. Yang, J. H. Lee, H.-K. Song, Y. Kim, S. K. Kwak and H. Ko, *J. Mater. Chem. A*, 2017, **5**, 2037-2044.
- 34 Y. Li, S. Niu, D. Rakov, Y. Wang, M. Cabán-Acevedo, S. Zheng, B. Song and P. Xu, *Nanoscale*, 2018, **10**, 7291-7297.
- 35 W. Niu and Y. Yang, *ACS Appl. Energy Mater.*, 2018, **1**, 2440-2445.
- 36 J. Kim, J. S. Kang, J. Jeong, Y. J. Son, M. J. Lee, J. Kang, A. Lim, H. S. Park and Y.-E. Sung, *J. Power Sources*, 2018, **396**, 213-219.
- 37 W. Xia, A. Mahmood, R. Zou and Q. Xu, *Energy Environ. Sci.*, 2015, **8**, 1837-1866.

- 38 Y. Zhao, Z. Song, X. Li, N. Cheng, S. Lawes and X. Sun, *Energy Storage Mater.*, 2016, **2**, 35-62.
- 39 S.-H. Hsu, C.-T. Li, H.-T. Chien, R. R. Salunkhe, N. Suzuki, Y. Yamauchi, K.-C. Ho and K. C.-W. Wu, *Sci. Rep.*, 2014, **4**, 6983.
- 40 M.-S. Wu, C.-Y. Chen, Y.-R. Chen and H.-C. Shih, *Electrochim. Acta*, 2016, **215**, 50-56.
- 41 X. Cui, Z. Xie and Y. Wang, *Nanoscale* 2016, **8**, 11984-11992.
- 42 J. E. Chen, M.-S. Fan, Y.-L. Chen, Y.-H. Deng, J. H. Kim, H. R. Alamri, Z. A. Allothman, Y. Yamauchi, K.-C. Ho and K. C.-W. Wu, *Chem. Eur. J.*, 2017, **23**, 13284-13288.
- 43 Z. Xie, X. Cui, W. Xu and Y. Wang, *Electrochim. Acta*, 2017, **229**, 361-370.
- 44 T.-Y. Chen, Y.-J. Huang, C.-T. Li, C.-W. Kung, R. Vittal and K.-C. Ho, *Nano Energy*, 2017, **32**, 19-27.
- 45 S. H. Ahn, C. H. Lee, M. S. Kim, S. A. Kim, B. Kang, H.-e. Kim, S. U. Lee and J. H. Bang, *J. Phys. Chem. C*, 2017, **121**, 27332-27343.
- 46 W. Chaikittisilp, M. Hu, H. Wang, H.-S. Huang, T. Fujita, K. C.-W. Wu, L.-C. Chen, Y. Yamauchi and K. Ariga, *Chem. Commun.*, 2012, **48**, 7259-7261.
- 47 W. Chaikittisilp, K. Ariga and Y. Yamauchi, *J. Mater. Chem. A*, 2013, **1**, 14-19.
- 48 J. Tang, R. R. Salunkhe, J. Liu, N. L. Torad, M. Imura, S. Furukawa and Y. Yamauchi, *J. Am. Chem. Soc.*, 2015, **137**, 1572-1580.
- 49 K. Shen, X. Chen, J. Chen and Y. Li, *ACS Catal.*, 2016, **6**, 5887-5903.
- 50 Y. V. Kaneti, J. Tang, R. R. Salunkhe, X. Jiang, A. Yu, K. C.-W. Wu and Y. Yamauchi, *Adv. Mater.*, 2017, **29**, 1604898.
- 51 A. Aijaz, N. Fujiwara and Q. Xu, *J. Am. Chem. Soc.*, 2014, **136**, 6790-

6793.

- 52 L. Zhang, Z. Su, F. Jiang, L. Yang, J. Qian, Y. Zhou, W. Li and M. Hong, *Nanoscale*, 2014, **6**, 6590-6602.
- 53 D. Y. Chung, K. J. Lee, S.-H. Yu, M. Kim, S. Y. Lee, O.-H. Kim, H.-J. Park and Y.-E. Sung, *Adv. Energy Mater.*, 2015, **5**, 1401309.
- 54 Q. Ren, H. Wang, X.-F. Lu, Y.-X. Tong and G.-R. Li, *Adv. Sci.*, 2017, **4**, 1700515.
- 55 X. Sun, Y. Li, J. Dou, D. Shen and M. Wei, *J. Power Sources*, 2016, **322**, 93-98.
- 56 B. Zhao, H. Huang, P. Jiang, H. Zhao, X. Huang, P. Shen, D. Wu, R. Fu and S. Tan, *J. Phys. Chem. C*, 2011, **115**, 22615-22621.
- 57 F. Caturla, M. Molina-Sabio and F. Rodríguez-Reinoso, *Carbon*, 1991, **7**, 999-1007.
- 58 Z. Hu, M. P. Srinivasan and Y. Ni, *Carbon*, 2001, **39**, 877-886.
- 59 J. Pampel and T.-P. Fellingner, *Adv. Energy Mater.*, 2016, **6**, 1502389.
- 60 D. Y. Chung, Y. J. Son, J. M. Yoo, J. S. Kang, C.-Y. Ahn, S. Park and Y.-E. Sung, *ACS Appl. Mater. Interfaces*, 2017, **9**, 41303-41313.
- 61 Z.-L. Yu, G.-C. Li, N. Felcher, N. Yang, Z.-Y. Ma, X. Wang, M. Antonietti and S.-H. Yu, *Angew. Chem. Int. Ed.*, 2016, **55**, 14623-14627.
- 62 W. Li, X. Wu, H. Liu, J. Chen, W. Tang and Y. Chen, *New J. Chem.*, 2015, **39**, 7060-7065.
- 63 G. Zheng, S. de Marchi, V. López-Puente, K. Sentosun, L. Polavarapu, I. Pérez-Juste, E. H. Hill, S. Bals, L. M. Liz-Marzán, I. Pastoriza-Santos and J. Pérez-Juste, *Small*, 2016, **12**, 3935-3943.
- 64 H. Lee, S. M. Dellatore, W. M. Miller and P. B. Messersmith, *Science*, 2007, **318**, 426-430.
- 65 D. Y. Chung, S. W. Jun, G. Yoon, S. G. Kwon, D. Y. Shin, P. Seo, J. M.

- Yoo, H. Shin, Y.-H. Chung, H. Kim, B. S. Mun, K.-S. Lee, N.-S. Lee, S. J. Yoo, D.-H. Lim, K. Kang, Y.-E. Sung and T. Hyeon, *J. Am. Chem. Soc.*, 2015, **137**, 15478-15485.
- 66 J. Zhong, J.-J. Deng, B.-H. Mao, T. Xie, X.-H. Sun, Z.-G. Mou, C.-H. Hong, P. Yang and S.-D. Wang, *Carbon*, 2012, **50**, 321-341.
- 67 J. Zhong, H. Zhang, X. Sun and S.-T. Lee, *Adv. Mater.*, 2014, **26**, 7786-7806.
- 68 N. Dwivedi, R. J. Yeo, N. Satyanarayana, S. Kundu, S. Tripathy and C. S. Bhatia, *Sci. Rep.*, 2015, **5**, 7772.
- 69 S.-H. Yu, D. J. Lee, M. Park, S. G. Kwon, H. S. Lee, A. Jin, K.-S. Lee, J. E. Lee, M. H. Oh, K. Kang, Y.-E. Sung and T. Hyeon, *J. Am. Chem. Soc.*, 2015, **137**, 11954-11961.
- 70 T. Sharifi, G. Hu, X. Jia and T. Wågberg, *ACS Nano*, 2012, **6**, 8904-8912.
- 71 D. Guo, R. Shibuya, C. Akiba, S. Saji, T. Kondo and J. Nakamura, *Science*, 2016, **351**, 361-365.
- 72 N. Papageorgiou, W. F. Maier and M. Grätzel, *J. Electrochem. Soc.*, 1997, **144**, 876-884.
- 73 A. Hauch and A. Georg, *Electrochim. Acta*, 2001, **46**, 3457-3466.
- 74 J. S. Kang, J. Kim, J.-Y. Kim, M. J. Lee, J. Kang, Y. J. Son, J. Jeong, S. H. Park, M. J. Ko and Y.-E. Sung, *ACS Appl. Mater. Interfaces*, 2018, **10**, 8611-8620.
- 75 L. Kavan, J. H. Yum and M. Grätzel, *ACS Nano*, 2011, **5**, 165-172.
- 76 J. D. Roy-Mayhew, D. J. Bozym, C. Punckt and I. A. Aksay, *ACS Nano*, 2010, **4**, 6203-6211.
- 77 D.-S. Yang, C. Kim, M. Y. Song, H.-Y. Park, J. C. Kim, J.-J. Lee, M. J. Ju and J.-S. Yu, *J. Phys. Chem. C*, 2014, **118**, 16694-16702.
- 78 Y. Marcus, *Chem. Rev.*, 1988, **88**, 1475-1498.

- 79 E. R. Nightingale, *J. Phys. Chem.*, 1959, **63**, 1381-1387.
- 80 J. Chmiola, G. Yushin, Y. Gogotsi, C. Portet, P. Simon and P. L. Taberna, *Science*, 2006, **313**, 1760-1763.
- 81 J. S. Kang, M.-A. Park, J.-Y. Kim, S. H. Park, D. Y. Chung, S.-H. Yu, J. Kim, J. Park, J.-W. Choi, K. J. Lee, J. Jeong, M. J. Ko, K.-S. Ahn and Y.-E. Sung, *Sci. Rep.*, 2015, **5**, 10450.
- 82 Y. Hou, D. Wang, X. H. Yang, W. Q. Fang, B. Zhang, H. F. Wang, G. Z. Lu, P. Hu, H. J. Zhao and H. G. Yang, *Nat. Commun.*, 2013, **4**, 1583.
- 83 V. R. Stamenkovic, B. S. Mun, M. Arenz, K. J. J. Mayrhofer, C. A. Lucas, G. Wang, P. N. Ross and N. M. Markovic, *Nat. Mater.*, 2007, **6**, 241-247.
- 84 V. R. Stamenkovic, D. Strmcnik, P. P. Lopes and N. M. Markovic, *Nat. Mater.*, 2017, **16**, 57-69.
- 85 D. Wang, J. Jiang, H.-F. Wang and P. Hu, *ACS Catal.*, 2016, **6**, 733-741.
- 86 A. C. Ferrari and J. Robertson, *Phys. Rev. B*, 2000, **61**, 14095-14107.
- 87 J. D. Wilcox, M. M. Doeff, M. Marcinek and R. Kostecki, *J. Electrochem. Soc.*, 2007, **154**, A389-A395.
- 88 Z. Zhu, F. Cheng and J. Chen, *J. Mater. Chem. A*, 2013, **1**, 9484-9490.
- 89 N. Baro, Jaidev and S. Ramaprabhu, *RSC Adv.*, 2016, **6**, 96109-96120.
- 90 P. M. Sommeling, B. C. O'Regan, R. R. Haswell, H. J. P. Smit, N. J. Bakker, J. J. T. Smits, J. M. Kroon and J. A. M. Roosmalen, *J. Phys. Chem. B*, 2006, **110**, 19191-19197.
- 91 J. S. Kang, J. Kang, D. Y. Chung, Y. J. Son, S. Kim, S. Kim, J. Kim, J. Jeong, M. J. Lee, H. Shin, S. Park, S. J. Yoo, M. J. Ko, J. Yoon and Y.-E. Sung, *J. Mater. Chem. A*, 2018, **6**, 20170-20183.

국문초록

고성능 염료감응태양전지를 위한
금속유기구조체 유래의 질소가 도핑된
탄소 전기촉매의 기공성 조절

서울대학교 대학원

화학생물공학부 에너지환경화학융합기술전공

강지호

금속유기구조체-유래 탄소 물질은 다양한 전기화학 에너지 응용을 위한 촉매로 널리 사용되어 왔으며, 열 탄화 아연-2-메틸이미다졸 (ZIF-8) 은 넓은 표면적의 미세 다공성 구조로 인해 특히 높은 성능을 보여왔다. 그러나, 메조스코픽 염료감응태양전지의 트리요오드화물과 같이 부피가 큰 화학 종이 있을 때, 탄화 ZIF-8 의 작은 기공 크기는 물질 전달에 상당한 제한을 야기하며 결과적으로 저조한 성능의 원인이 된다. 이러한 문제를 해결하기 위해, 이 연구에서는 열 탄화 과정에서 아연의 ZIF-8 속 체류 시간을 늘림으로써 ZIF-8-유래 탄소의

기공 크기를 확대하는 간단한 전략을 소개한다. 기화된 아연 종들이 빠져나가는 것을 지연시킬 목적으로 ZIF-8 의 표면에 도입된 얇고 균일한 폴리도파민 껍질은, 기공 크기를 미세공극에서 중기공극 범위로 극적으로 증가시켰다. 기공성-맞춤형 탄화 ZIF-8 은 트리요오드화물 환원 반응에서 훌륭한 전기촉매적 성능을 자랑하였고, 염료감응전지상대 전극에 적용되었 때 9.03 % 에 이르는 에너지 전환 효율을 달성할 수 있었다. 이는 백금 기반의 대조군에 비해 우수할 뿐만 아니라, 탄소 계 전기 촉매를 사용하는 염료감응태양전지로부터 얻어진 최고 성능들 중 하나이다.

핵심어: 염료감응태양전지, 상대전극, 트리요오드화물 환원 반응, 물질 전달 저항, 금속유기구조체, 기공성 조절, 폴리도파민

학번: 2017-28143